OPEN ACCESS
IOP Publishing
Journal of Physics: Condensed Matter
J. Phys.: Condens. Matter **36** (2024) 503001 (21pp)
https://doi.org/10.1088/1361-648X/ad7cb3

Topical Review

A brief review of microstructure design in transition metal-based magnetocaloric materials

Yong Gong[1], **Xuefei Miao**[1,*], **Fengjiao Qian**[2], **Feng Xu**[1] **and Luana Caron**[3,4,*]

[1] School of Materials Science and Engineering, Nanjing University of Science and Technology, 210094 Nanjing, People's Republic of China
[2] College of Physics, Nanjing University of Aeronautics and Astronautics, 210016 Nanjing, People's Republic of China
[3] Department of Physics, Bielefeld University, 33501 Bielefeld, Germany
[4] Helmholtz-Zentrum Berlin für Materialien und Energie, 12489 Berlin, Germany

E-mail: xuefeimiao@njust.edu.cn and luana.caron@uni-bielefeld.de

Received 23 April 2024, revised 13 August 2024
Accepted for publication 18 September 2024
Published 27 September 2024

Abstract
Magnetic cooling, a solid-state refrigeration technology based on the magnetocaloric effect, has attracted significant attention in space cooling due to its high energy-efficiency and environmental friendliness. Transition metal-based magnetocaloric materials (MCMs) with the merit of low-cost have emerged as promising candidates for efficient magnetic refrigeration applications. This review explores the intricate relationship between microstructure and multiple properties (e.g. magnetocaloric properties, mechanical stability, thermal conductivity, and functional reversibility) of these materials. A variety of microstructural manipulation approaches (e.g. crystallographic texture, precipitates, micropores, atomic-scale defects, size effect, and composites) are examined for their effects on the comprehensive performance of MCMs. We show that microstructure design provides an effective tool to achieve excellent performance in multiple aspects, which may facilitate the commercialization of transition-metal based MCMs.

Keywords: magnetocaloric effect, microstructure design, magnetic phase transition, thermal hysteresis, mechanical stability, thermal conductivity

1. Introduction

With the continuous development of modern society, the rising energy consumption has raised concerns regarding energy scarcity and global warming. It is worth noting that the energy consumption associated with space cooling is increasing rapidly and accounts for more than 15% of the global energy consumption [1, 2]. Space cooling is mainly based on the conventional vapor-compression technique that utilizes ozone-depleting refrigerants [3]. Magnetic cooling, a solid-state refrigeration technique based on the magnetocaloric effect (MCE), has developed rapidly over the past few decades and is currently a technology with great potential to meet the urgent global demand for energy-efficient eco-friendly thermal management [4, 5]. Magnetic refrigeration is theoretically predicted to be 20%–30% more energy-efficient than vapor-compression refrigeration [6–9]. In addition, the refrigerants used in magnetic cooling are eco-friendly solid

* Authors to whom any correspondence should be addressed.

materials that eliminate the emission of ozone-depletion or greenhouse gases [10], can be fully recovered and reused or safely disposed of. Apart from space cooling, magnetocaloric materials (MCM) also find new applications in magnetic hyperthermia [11], hydrogen liquefaction [12–15] and thermomagnetic power generation [16, 17]. The thermodynamics and magnetocaloric prototypes are comprehensively described in recent review articles and books [5, 8, 17–21].

The MCE is fundamental to the operation of magnetic refrigeration systems, which is manifested by the changes in temperature and entropy of the MCM when subjected to a varying external magnetic field [22–24]. This effect is particularly pronounced in the vicinity of magnetic phase transitions due to the strong coupling between the spin, lattice, and electronic degrees of freedom [21, 25]. The magnitude of the MCE is usually characterized by the isothermal entropy change ΔS_{iso} and the adiabatic temperature change ΔT_{ad}. Since magnetic refrigeration systems are operated in continuous thermal cycles, reversible ΔS_{iso} and ΔT_{ad} are crucial for the implementation of MCMs. The reversible ΔS_{iso} defines the amount of transferred heat during consecutive cooling cycles, while the reversible ΔT_{ad} determines the temperature span of the magnetic refrigeration system. MCMs with large reversible ΔS_{iso} and ΔT_{ad} values under a field change of less than 1.5 T are ideal for magnetic refrigeration applications since Nd–Fe–B permanent magnets are usually used as the field source in magnetic refrigeration systems [18, 26].

The rare-earth metal Gd is the benchmark magnetocaloric material, and has been widely used in magnetocaloric systems prototypes [18, 26]. However, the element's rarity impedes its commercialization. Although less rare earth is contained in rare-earth based alloys such as $Gd_5(Si_2Ge_2)$, the criticality and high cost make rare-earth based MCMs unfavorable for practical applications in magnetic refrigeration. Besides that, the poor corrosion and oxidation resistance of rare-earth based MCMs pose challenges to long-term stability [27]. Compared with rare-earth based MCMs, transition-metal based MCMs with the merit of low-cost and better stability are more promising for practical applications, especially those showing a first-order magnetic transition (FOMT), e.g. $(Mn,Fe)_2(P,X)$ (X = Si, Ge, As) [28, 29], $La(Fe,Si)_{13}$ [30, 31], Mn*MX* (M = Co, Ni; X = Ge, Si) [32, 33], and Heusler-type NiMn*X* (X = In, Ga, Sn, Sb, Ti) [34–36] alloys. The FOMT is usually accompanied by a structural reconfiguration and charge redistribution [37, 38]. Therefore, apart from the magnetic entropy change (ΔS_{mag}), lattice (ΔS_{lat}) and electron (ΔS_e) entropy changes also make major contributions to the total ΔS_{iso} of FOMT materials, leading to the so-called giant MCE. Nevertheless, the nucleation and growth of new phases during the FOMT cause energy dissipation, which leads to irreversibility of the FOMT and hence to the degradation of the reversible ΔS_{iso} and ΔT_{ad} during consecutive cooling cycles [39]. Recent progress in the transition-metal based MCMs can be found in the reviews from Chaudhary [4] and Law *et al* [40, 41].

It should be noted that some non-magnetocaloric properties, i.e. thermal conductivity, corrosion resistance, mechanical stability, are also crucial to MCMs. The operating frequency of a magnetic refrigeration system is limited by the heat exchange between the fluid and MCMs [42], which requires high thermal conductivity λ for MCMs as well as a large surface area involved in the heat exchange. The latter may be realized by manufacturing MCMs into specific geometries, e.g. thin plates [43, 44], sphere-packed beds [45] and honeycomb-like micro-channels [46–48]. Besides that, MCMs should ensure good magnetocaloric performance, structural integrity and resistance to fatigue over millions of thermal and field cycles [49]. The corrosion resistance also needs to be considered due to the long-term contact between MCMs and heat-exchange fluids [50]. Additionally, in order to reduce the cost and environmental impact, the constituent elements of MCMs should be abundant and non-toxic. The selection criteria of MCMs have been comprehensively reviewed by Gottschall *et al* [51].

Lots of efforts have been made to optimize the magnetocaloric and non-magnetocaloric properties of MCMs via compositional variation or microstructural manipulation. For example, the thermal hysteresis (ΔT_{hys}) of the FOMT in the Mn*MX* and Heusler-type NiMn*X* alloys can be reduced by improving the structural compatibility between the austenite and martensite phases through composition adjustment [35, 52–56]. The ΔT_{hys} may also be diminished by the construction of a textured microstructure [57, 58] as well as the introduction of multiple structural defects in the MCMs which results in a reduced energy barrier of the nucleation process during the FOMTs [50, 59–61]. The design and fabrication of magnetocaloric composites can also lead to significant enhancement of the thermal conductivity, corrosion resistance and mechanical stability [43, 62–76]. This review article aims at demonstrating the importance of microstructure design in boosting the magnetocaloric, thermal and mechanical properties of MCMs. A variety of microstructural manipulation approaches (e.g. crystallographic texture, precipitates, micropores, atomic-scale defects, size effect, and magnetocaloric composites) will be highlighted, as illustrated in figure 1. The present work may offer researchers new strategies for the design and optimization of high-performance MCMs, which facilitates the commercialization of magnetocaloric-based refrigeration and energy conversion techniques.

2. Microstructure design

2.1. Crystallographic texture

The minimum magnetic field required to drive a completely reversible FOMT strongly depends on the transition width (i.e. sharpness of the FOMT) and thermal hysteresis [54, 55, 82, 83]. The significant structural deformation across the FOMT brings about considerable transition-induced stress in MCMs, which in turn affects the FOMT characteristics. Gottschall *et al* [84] studied the stress-coupling mechanism for FOMTs by finite-element simulations. They constructed an artificial MCM with 10 × 10 × 10 individual grains. The transition temperature in each artificial grain is slightly

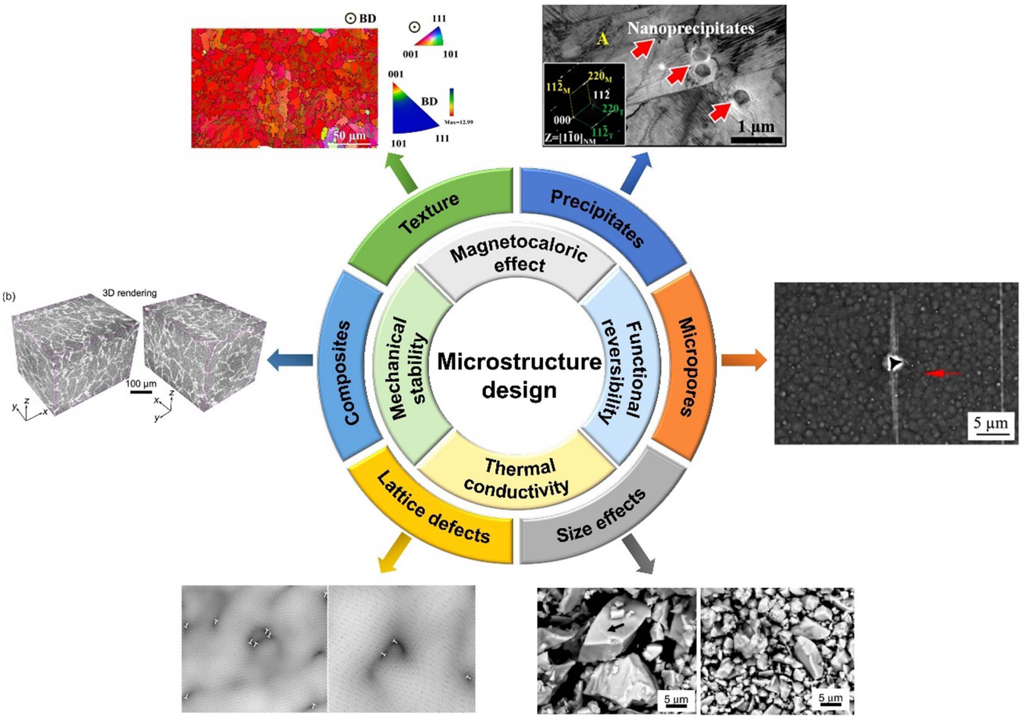

Figure 1. Different microstructure design strategies employed to tailor the magnetocaloric, thermal and mechanical properties of MCMs. Reprinted from [76], Copyright (2023), with permission from Elsevier. Reprinted from [77], Copyright (2024), with permission from Elsevier. Reprinted from [78], with the permission of AIP Publishing. Reproduced from [79]. CC BY 4.0. Reprinted from [80], Copyright (2012), with permission from Elsevier. Reproduced from [81]. CC BY 4.0.

different and follows a Gaussian distribution. They found that the FOMT tends to start from the corner of the ensemble since the artificial grains at the corner are less constrained by the neighboring grains. Due to the significant structural reconfiguration, large stress is accumulated across the FOMT, which inhibits the transformation of the neighboring grains. With an increase in the stress-coupling constant (i.e. the sensitivity of the transition temperature to stress), the FOMT is broadened (figure 2(a)). Besides that, they explored the effect of grain orientation on the FOMT when anisotropic structural deformation occurs across the FOMT. As shown in figure 2(b), a transition-induced stress up to 0.6 GPa is built in the isotropic MCM, resulting in a broader FOMT than that in the powdered counterpart where the stress-coupling effect is absent. They found that in the artificial MCM with a strong crystallographic texture, the synergistic deformation between neighboring grains leads to a sharp FOMT. Consequently, finite-element simulation predicts that the width of a FOMT can be decreased by constructing crystallographic texture in MCMs, which improves the reversibility of FOMTs at low magnetic fields.

The effect of crystallographic texture on the characteristics of the FOMT has recently been experimentally demonstrated in MnNiGe-based MCMs. MnNiGe-based alloys undergo a FOMT from the ferromagnetic Ni_2In-type hexagonal austenite (space group *P6$_3$/mmc*) to the paramagnetic TiNiSi-type orthorhombic martensite (space group *Pnma*). There is a significant anisotropic structural deformation across the FOMT, where the martensitic unit cell shrinks by ∼10.28% along the *a* axis while it elongates by ∼8.77% along the *b* axis, resulting in a volume change of up to 4%. Such severe anisotropic structural deformations cause stress concentration, which leads to a large thermal hysteresis, a broadening of the transition and widespread structural fracture. As presented in figures 2(c)–(e), the textured sample shows a reduced ΔT_{hys} (by ∼42%), narrower transition width and enhanced reversible ΔS_{iso} (increased by ∼87.5%) compared to its non-textured counterpart. Additionally, the textured MnNiGe-based MCMs display significantly improved mechanical stability, and remain intact after 400 thermal cycles. Guo *et al* [85] claimed that the improved reversible MCE and mechanical stability is due to the synergistic deformation between neighboring grains in the textured samples, which relieves stress concentration and reduces the energy barrier of the FOMT. Gong *et al* [86] also reported the enhancement of magnetocaloric performance in $(Mn,Fe)_5Si_3$ alloys by the introduction of crystallographic texture. The textured $MnFe_4Si_3$ alloy shows a maximum ΔS_{iso} of -2.47 Jkg^{-1} K^{-1} under a ΔH of 2 T, which is comparable to that of single crystals (-2.90 Jkg^{-1} K^{-1}) and higher than that of powdered samples (-2.0 Jkg^{-1} K^{-1}) [86].

The most common strategy to introduce crystallographic texture in MCMs is to use directional solidification techniques [86, 88, 89], which establish a unidirectional temperature gradient that allows the liquid metal to solidify and crystalize along the temperature gradient direction. For instance,

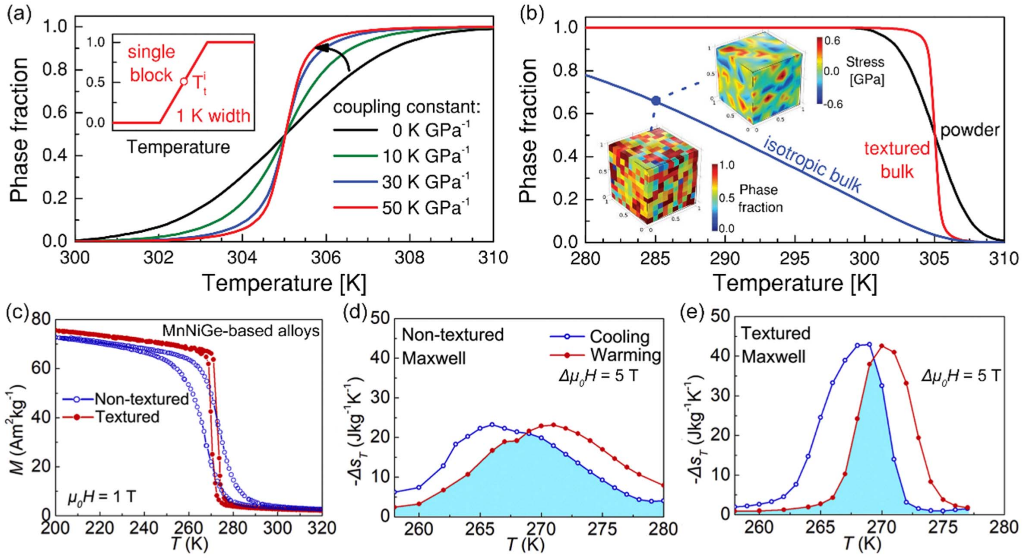

Figure 2. Temperature dependence of the simulated transformation in (a) isotropic bulk with different stress-coupling constants and (b) isotropic bulk, textured bulk and powder under a stress-coupling constant of 50 $KGPa^{-1}$. [84] John Wiley & Sons. (Copyright © 2017 WILEY-VCH Verlag GmbH & Co. KGaA, Weinheim). Temperature dependence of the (c) magnetization and (d), (e) isothermal entropy change in textured and non-textured MnNiGe-based alloys. Reprinted from [85], Copyright (2024), with permission from Elsevier.

directionally-solidified MnNiGe-based MCMs exhibit a dense and textured microstructure as evidenced by x-ray diffraction (XRD, figure 3(a)), scanning electron microscope (SEM, figure 3(b)) and electron back-scattered diffraction (EBSD, figure 3(c)).

Recently, addictive manufacturing has proven to be a new way to obtain crystallographic texture in MCMs due to the nonequilibrium solidification induced by extremely fast cooling rates [90]. Laser powder bed fusion (L-PBF) [77] was employed to fabricate $Ni_{40}Co_6Mn_{43}Sn_{11}$ magnetic shape memory alloys (figure 3(d)). Compared to the directional solidification technique, the large cooling rate during the L-PBF leads to the formation of dendrites due to the micro-segregation caused by nonequilibrium solidification (figure 3(e)). The large temperature gradient induced by the supercooling in the melt pool favors grain growth along the $<001>_A$ direction. As a result, columnar grains grow towards the middle of the melt pool, which leads to a strong $<001>_A$ texture along the building direction (figure 3(f)).

In addition to solidification-based fabrication techniques, it is also possible to exploit the magnetocrystalline anisotropy itself to obtain crystallographic texture in MCMs via magnetic field alignment [87, 91]. Zhou *et al* [87] reported magnetic field-aligned Mn*MX*/In composites, where the ferromagnetic Mn*MX* particles embedded in the In matrix are aligned by the external magnetic field under a unidirectional pressure (figures 3(g) and (h)). The magnetocrystalline anisotropy of Mn*MX* alloys leads to the preferred orientation of Mn*MX* particles along the $<001>$ crystallographic direction induced by the static magnetic field (figure 3(i)). Recently, Guo *et al* [91] prepared $<100>$-textured Mn*MX*/epoxy composites by magnetic field-assisted dynamic self-assembly of ferromagnetic Mn*MX* particles. The application of static or dynamic magnetic field offers the possibility of tuning the texture direction in MCMs as long as long-range magnetic order is present in the compounds during the process.

2.2. Precipitates

A FOMT is characterized by the nucleation and growth of a new phase, which is influenced by the presence of multi-scale precipitates [78, 92–95]. Recently, Liang *et al* [78] introduced different amounts of Dy in the Heusler-type $Ni_{54}Mn_{25}Ga_{21-x}Dy_x$ alloys with $x = 0$, 0.01, 0.03, and 0.05 (refer to Dy0, Dy0.1, Dy0.3, and Dy0.5). Transmission electron microscopy (TEM) analyses indicate the appearance of precipitates with diameters between 200 and 250 nm in the Dy0.1 sample (figures 4(a) and (b)), which is suggested to be the $DyNi_4Ga$ phase by selected area electron diffraction (inset of figure 4(b)) and energy dispersive spectrometry (EDS, figure 4(c)). The mismatch of local atoms and atom shuffling are inevitable near the precipitate/matrix interface, resulting in misfit dislocations and partial strain field fluctuation. The induced strain fields can assist the process of nucleation by reducing the energy barrier of the martensitic transformation. As a result, the ΔT_{hys} is reduced from 13 K in the Dy0 sample to 6.2 K in the Dy5 sample (figures 4(d) and (e)).

However, the presence of precipitates may also cause adverse effects on the FOMT of MCMs. In Tb micro-alloyed Ni–Mn–Ga MCMs [92], the presence of dispersedly-distributed precipitates with an average size of about 10 μm induces an inhomogeneous stress field around the precipitates (figures 5(a) and (b)). The inhomogeneous internal stress field causes the variation of the local transition temperature due to the strong stress-coupling effect of the FOMT. Therefore, the Tb precipitate-containing Ni–Mn–Ga MCMs

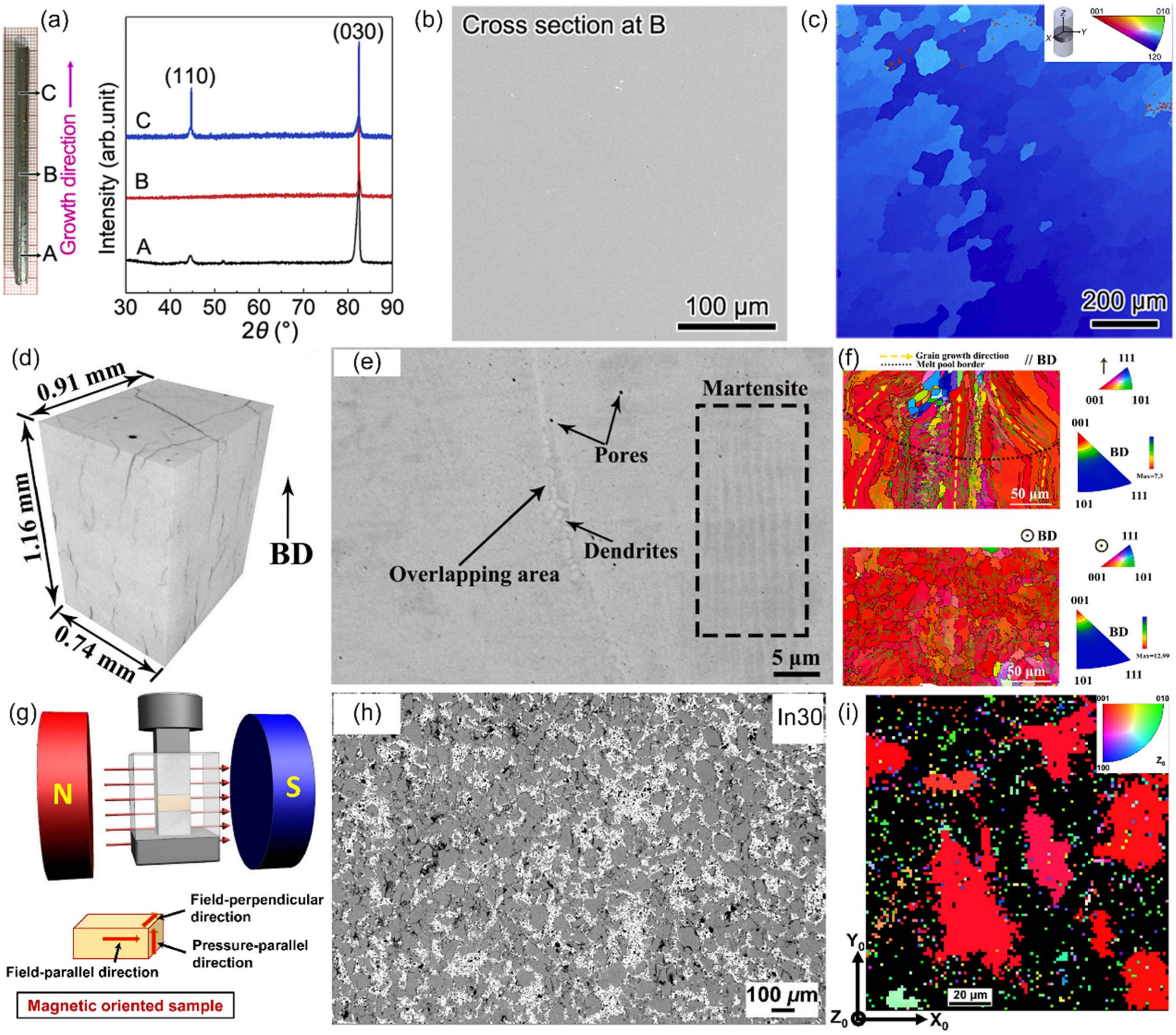

Figure 3. (a) XRD patterns, (b) SEM image and (c) EBSD orientation map of directionally-solidified MnNiGe-based alloy. Reprinted from [85], Copyright (2024), with permission from Elsevier. (d) 3D-CT, (e) SEM and (f) EBSD orientation maps of L-PBFed Ni–Co–Mn–Sn alloy. Reprinted from [77], Copyright (2024), with permission from Elsevier. (g) Schematic diagram of the magnetic field alignment process. (h) SEM image and (i) EBSD orientation map of the field-aligned MnM*X*/In composite. Reprinted from [87], Copyright (2022), with permission from Elsevier.

exhibit broadened FOMT (figures 5(c) and (d)), in strong contrast to the Dy-alloyed Ni–Mn–Ga alloys (figure 4).

A similar behavior has also been observed in Ni–Mn–In MCMs [94], where the thermal hysteresis and transition width are considerably increased by Fe doping (figures 5(e) and (f)). The variation in the macroscopic characteristics of the FOMT has been attributed to the formation of nano-scaled precipitates in the matrix (figures 5(g)–(i)). The homogeneously distributed Fe-rich nano-scale precipitates generate intense stress fields and elevate the energy barrier of the growth process of the nucleated phase during the FOMT, resulting in the increase of thermal hysteresis and transition width [94].

2.3. Micropores

Introducing porosity is an effective approach to enhance the mechanical stability and reversibility of the FOMT in MCMs [96–98]. Lyubina *et al* [96] fabricated porous LaFeSi-based alloys by pressing $LaFe_{11.6}Si_{1.4}$ powders at 898 K for 2 min. A thermal hysteresis of 2.3 K appears in the conventional bulk sample (figure 6(a)) due to the substantial volume expansion that induces substantial local stress across the FOMT. The introduction of porosity partially removes the grain boundaries that restrain the volume expansion in the bulk sample. As a result, a thermal hysteresis as low as 0.5 K was obtained in the porous sample (figure 6(b)). Besides that, the stress concentration induced by the significant structural deformation across the FOMT is also a major challenge for the mechanical integrity of bulk samples. The conventional bulk sample exhibits a rapid degradation of ΔT_{ad} upon continuous temperature-field cycling due to the formation of microcracks and the sample loses its mechanical integrity after a mere 4 cycles (figure 6(c)). In contrast, the porous counterpart shows good magnetocaloric and mechanical stability during

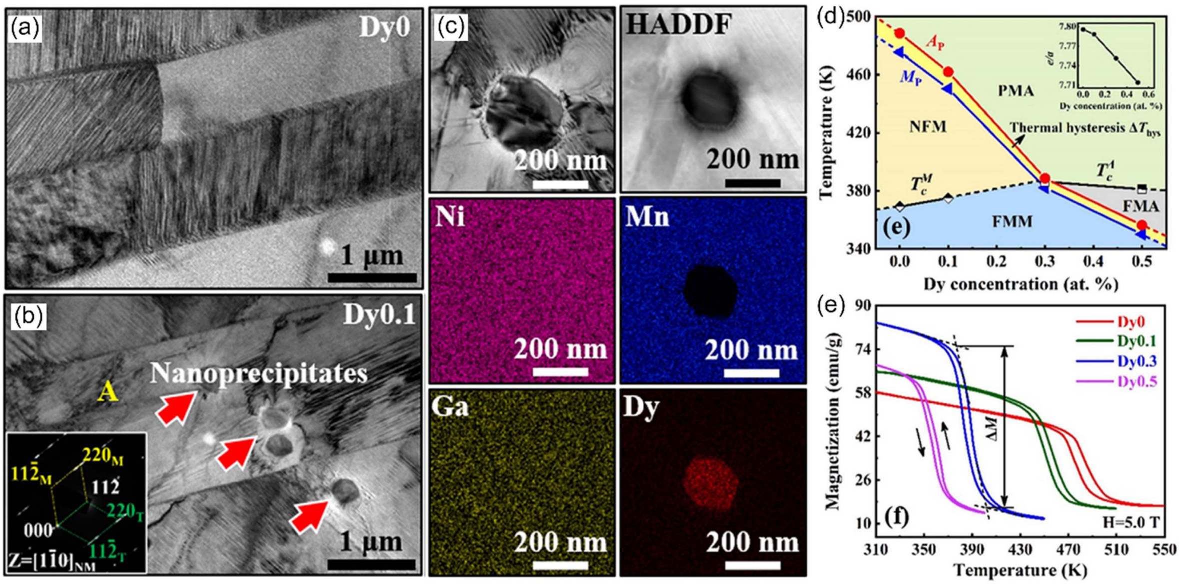

Figure 4. Bright field TEM images of (a) Dy0 and (b) Dy0.1 Ni–Mn–Ga alloys. (c) Bright TEM image and EDS elemental maps of the Dy0.3 alloy. (d) Magnetic and structural phase diagram of Dy-doped system. (e) Temperature dependence of magnetization in Dy-doped alloys under 5 T. Reprinted from [78], with the permission of AIP Publishing.

temperature-field cycles (figure 6(c)). The authors further performed *in situ* observation of the FOMT in the porous samples by magneto-optic Kerr microscopy (figures 6(g)–(i)). They found that the nucleation of the new phase always starts at the edge of small particles, suggesting that the FOMT is strongly inhibited by the internal constraint in large particles. Another strategy for introducing pores in bulk MCMs is to construct foam-shape structures by replication casting process [97]. Monroe *et al* [97] fabricated Ni–Mn–Sn–Co alloys with 50% porosity of 300–500 μm pores by solid-state replication of ammonium bicarbonate powder. The less constraints between neighboring grains in porous Ni–Mn–Sn–Co samples may lead to a smaller thermal hysteresis compared to conventional bulk counterparts [59].

Niemann *et al* [79] proposed to use nanoindentation to create well-defined pores in MCMs. They examined the effect of indentations on the nucleation and growth processes of the martensitic transformation in an epitaxial NiMnGa film. *In situ* SEM observations reveal that the martensitic transformation tends to start at the region close to the indentation (figures 7(a) and (b)). The underlying mechanism is suggested to be an increase in the transition temperature that is raised by the elastic stray field upon a plastic deformation [79]. Nevertheless, the tailoring effect of indentations decays with distance away from the indentation (figure 7(c)). Niemann *et al* [79] predicted that the decrease in the local nucleation barrier by introducing indentations may lead to the desirable reduction of the thermal hysteresis in MCMs. Recently, Ghahfarokhi *et al* [99] performed a more systematic investigation on the effect of nanoindentations on the martensitic transformation of an epitaxial NiMnGa film. They carefully examined the nucleation and growth of the martensite in different zones around the indentations, i.e. residual impression zone, pile-ups and 200/500/1200 nm from pile-ups (figure 7(e)). Upon cooling the sample from the austenitic state, the martensite phase starts to nucleate in the outer side of the pile-ups and subsequently occurs in zones away from the pile-ups (figure 7(d)). The variation of the local transformation temperature results in the broadening of the transition in the indented film (figure 7(f)), while no noticeable change in the thermal hysteresis is observed as compared to the pristine film (figure 7(g)).

It is worth to point out that, while the introduction of pores on MCMs may result in easier nucleation of the new phase at the phase transition and therefore lower energy barrier and thermal hysteresis, it likely becomes detrimental for higher porosity ratios (sometimes up to 50%). The high porosity may increase the surface to volume ratio which favors better heat exchange. However, it may also cause a drastic pressure drop in regenerators and it ultimately means a lot less material will be under a magnetic field change which in turn leads to a much lower efficiency in a magnetic refrigeration cycle.

2.4. Size effect

The individual grains in a bulk MCM are not free to deform during the FOMT. They are always constrained by neighboring grains. The influence of the grain-boundary constraints on the characteristics of the FOMT has been revealed by Gottschall *et al* [84]. They observed a sharper FOMT in the La–Fe–Si and Mn–Fe–P–Si materials with a smaller particle size (figures 8(a) and (b)), while the Ni–Mn–In–Co material shows an opposite trend (figure 8(c)). On the other hand, they found that the thermal hysteresis increases with a reduction in the particle size for all three MCMs [84].

In contrast, Liu *et al* [80] reported a different dependence of the FOMT on particle size for La–Fe–Si MCMs as Gottschall *et al*. Liu *et al* [80] explored the transition

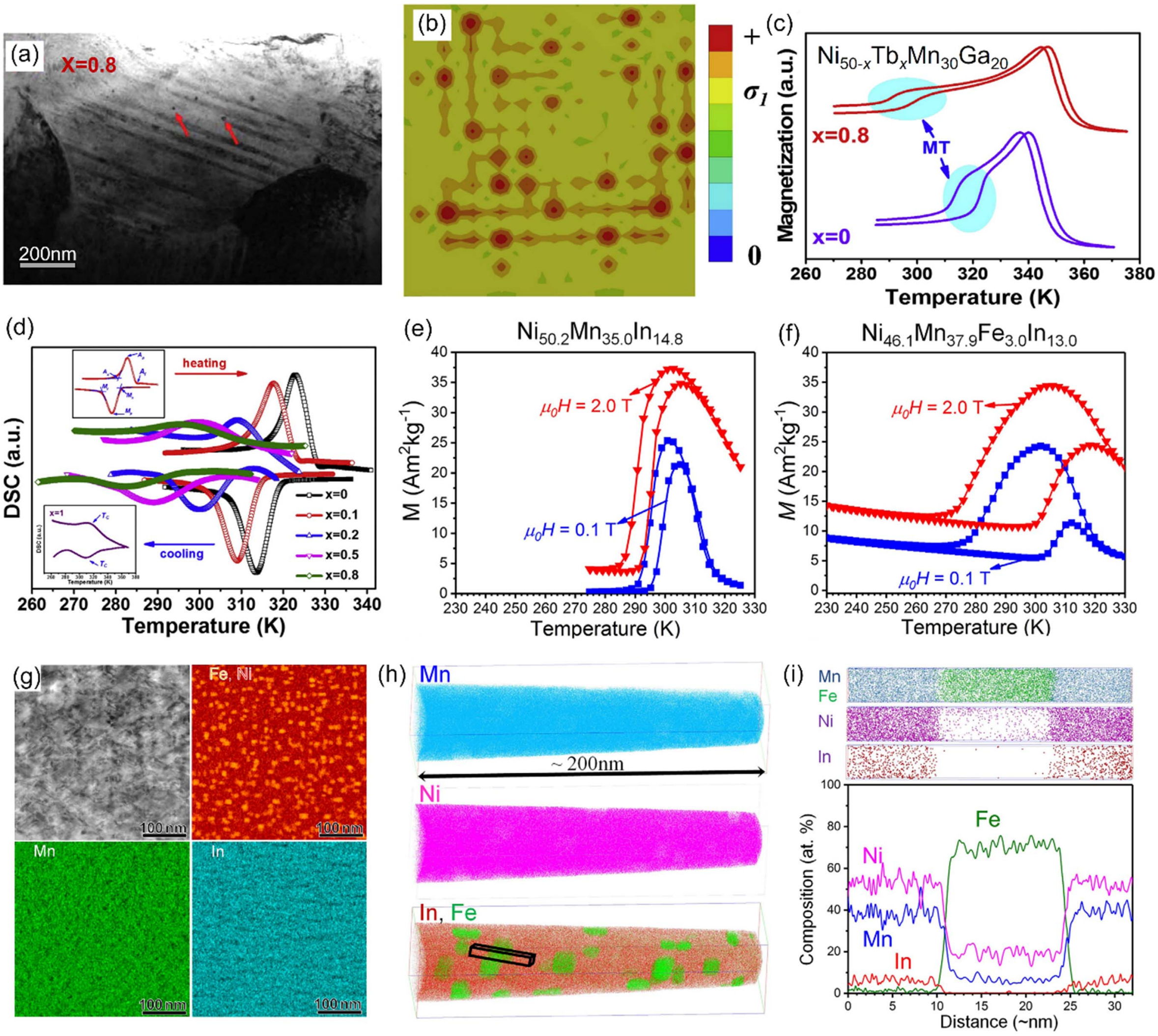

Figure 5. (a) Bright field TEM image of $Ni_{50-x}Tb_xMn_{30}Ga_{20}$ alloy with $x = 0.8$. (b) Simulation of local stress fields in the matrix with large amounts of nano-precipitates. (c) Magnetic and (d) calorimetric characterization results of $Ni_{50-x}Tb_xMn_{30}Ga_{20}$ alloys. Reprinted from [92], Copyright (2018), with permission from Elsevier. *M–T* curves of (e) Fe-free and (f) Fe-doped Ni–Mn–In alloys. (g), (h) TEM and EDS analyses of the Fe-doped Ni–Mn–In alloy. (i) Atom probe maps from the Fe-precipitate area. Reprinted from [94], Copyright (2018), with permission from Elsevier.

behavior and microstructure of La–Fe–Si particles after different ball-milling times. The FOMT becomes broadened with an increase in the ball-milling time (figure 9(a)), which may be due to the introduction of severe strain in the small particles after ball milling (figures 9(b) and (c)). A similar particle size-dependence of the FOMT has been reported by Zhang *et al* [100] in ball-milled Mn–Fe–P–Si MCMs (figure 9(d)). They obtained Mn–Fe–P–Si nanoparticles with an average size less than 100 nm after high-energy ball milling (figure 9(e)). The decrease in magnetization with reduced particle size is attributed to the presence of a magnetic dead layer in the amorphous shell of the nanoparticles (figure 9(f)).

Apart from particle size, grain size also strongly affects the FOMT in MCMs [50, 101, 102]. Liu *et al* [101] reported that the partial replacement of La by Ce in the $LaFe_{11}Si_2$ alloy brings about severe lattice distortions that may serve as hydrogen trapping sites in the subsequent hydrogenation process. Nano-sized (5–50 nm) $(La,Ce)Fe_{11}Si_2$ grains are formed to release the hydrogenation-induced internal stress (figure 10(a)). The nano-grains are further confirmed by the 3D atom probe, where no element segregation is detected. TEM analyses indicate a semi-coherent relationship between the nano-grains and matrix with considerable local strains (figure 10(b)). They claimed that the local strain field close to the boundaries between the nano-grains and matrix will largely reduce the nucleation energy barrier as well as provide nucleation sites during the FOMT [101]. As a consequence, the thermal and magnetic hysteresis are significantly reduced after grain refinement (figures 10(c)–(e)).

2.5. Atomic-scale defects

The characteristics of FOMT in MCMs may also be tailored by introducing atomic-scale defects. MnAs alloys show a FOMT where the ferromagnetic transition is coupled to a structural transition between a NiAs-type hexagonal α-phase

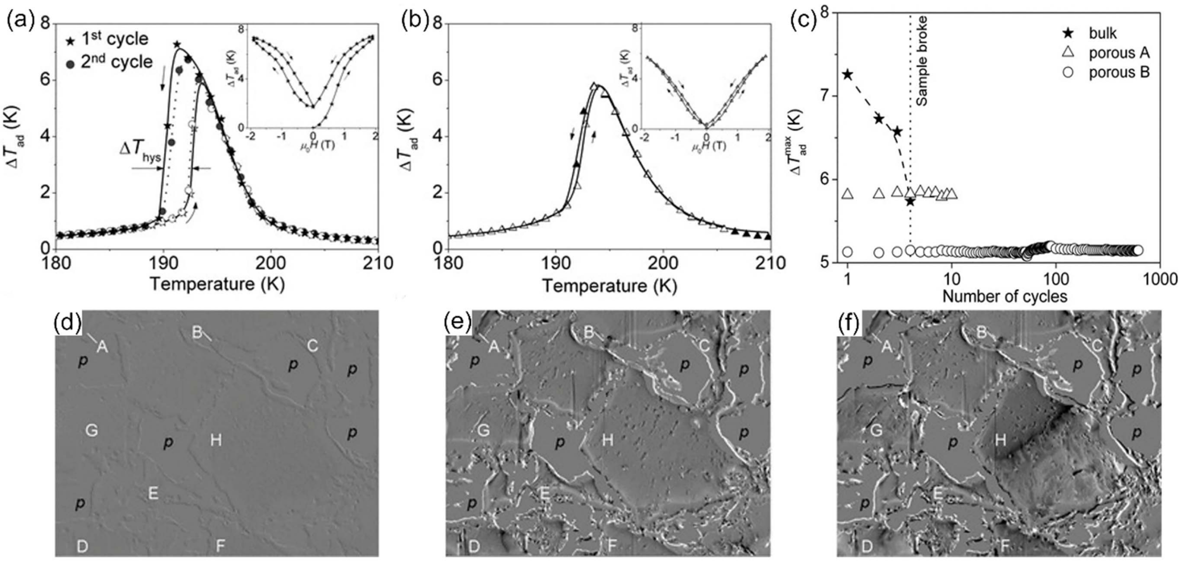

Figure 6. The ΔT_{ad} under a field change of 1.93 T in (a) conventional bulk and (b) porous $LaFe_{11.6}Si_{1.4}$ alloys. (f) The evolution of ΔT_{ad} after different temperature-field cycles for bulk and porous $LaFe_{11.6}Si_{1.4}$ alloys. Kerr images (d) above and (e,f) below the FOMT temperature of the porous $LaFe_{11.6}Si_{1.4}$ alloy. [96] John Wiley & Sons. (Copyright © 2010 WILEY-VCH Verlag GmbH & Co. KGaA, Weinheim).

and MnP-type orthorhombic β-phase. Trassinelli *et al* [103] investigated the irradiation effect of Ne^{9+} ions on the microstructure and FOMT of epitaxial MnAs thin films. With an increase in the ion fluence, the XRD peaks of both phases show a noticeable shift and broadening (figure 11(a)), suggesting the creation of large amounts of defects by highly charged ion bombardment. Magnetic force microscopy (MFM) revealed that stripe-like magnetic structures in the non-irradiated film are distorted by irradiation-induced defects (figure 11(b)). Interestingly, the thermal hysteresis disappears in the film undergoing irradiation of 1.5×10^{13} ion cm^{-2}, in strong contrast to the large thermal hysteresis of 5 K in the non-irradiated film (figure 11(c)). The authors claimed that the defects induced by the ion bombardment facilitate the nucleation process during the FOMT and hence lead to the suppression of thermal hysteresis [103].

Recently, Zhang *et al* [81] demonstrated that the FOMT and giant magnetocaloric properties of Heusler-type Ni–Co–Mn–Ti alloys can be regulated via defect engineering. They found that suction casting (SC) samples exhibit a sharper FOMT than arc melted samples (AM) (figure 12(a)). As a result, the total entropy change associated with the FOMT in the AM sample is improved by ~67% as compared with that in the SC samples (figure 12(b)). A large amount of quenched-in dislocations are observed in the AM samples (figures 12(c) and (d)), while the number of dislocations are considerably reduced in the SC samples (figures 12(e) and (f)). They attributed the lower dislocation density in the SC samples to the finer grain microstructure caused by the faster cooling rate during SC, which provides more grain boundaries for the coalescence and annihilation of dislocations [81]. The reduction of lattice defects in the SC samples is further confirmed by positron annihilation spectroscopy (PAS) results, where a faster change in the *S* and *W* parameters corresponds to a larger amount of lattice defects such as vacancies and dislocations (figure 12(g)). Therefore, the large amount of lattice defects in the AM samples reduce the energy barrier of nucleation and hence shift the FOMT towards higher temperatures, while the inhomogeneous distribution of the defects causes broadening of the transition. In contrast, SC samples with less lattice defects show a more uniform transformation with reduced transition width.

Recent studies indicate that magnetic frustration can contribute to the enhancement of magnetocaloric performance [104, 105]. A number of transition metal-based oxides with magnetic frustration display excellent magnetocaloric performance such as $Gd_2Ti_2O_7$ [106], $GdCrTiO_5$ [107] and $GdTaO_4$ [108]. Zhang *et al* [106] systematically investigated the structural and magnetic properties of geometrically frustrated $Gd_2Ti_2O_7$ oxide. Figure 13(a) shows the pyrochlore crystal structure of the $Gd_2Ti_2O_7$ oxide, where the Gd atoms occupy the 16*c* sites and the Ti atoms are on the 16*d* sites. Two magnetic phase transitions are observed around Néel temperatures T_{N1} and T_{N2} (figure 13(b)). The phase transition behavior is not considerably changed with an increase in the external magnetic field, indicating the presence of a strong AFM interaction induced by the magnetic frustration. The frustration results in an infinite degeneracy on the magnetic ground state, which corresponds to the existence of a large number of local zero-energy modes [109, 110]. Although the $Gd_2Ti_2O_7$ oxide undergoes a second-order magnetic phase transition (as suggested by the Arrot curves in figure 13(d)), it shows a relatively large isothermal entropy change (figure 13(e)). Additionally, Das *et al* [107] demonstrated the presence of magnetic frustration in $GdCrTiO_5$, which is originated from competing magnetic exchange interactions between two magnetic sublattices. The Gd moments are antiferromagnetically ordered below 0.9 K, while the Cr moments do not show any long-range magnetic ordering

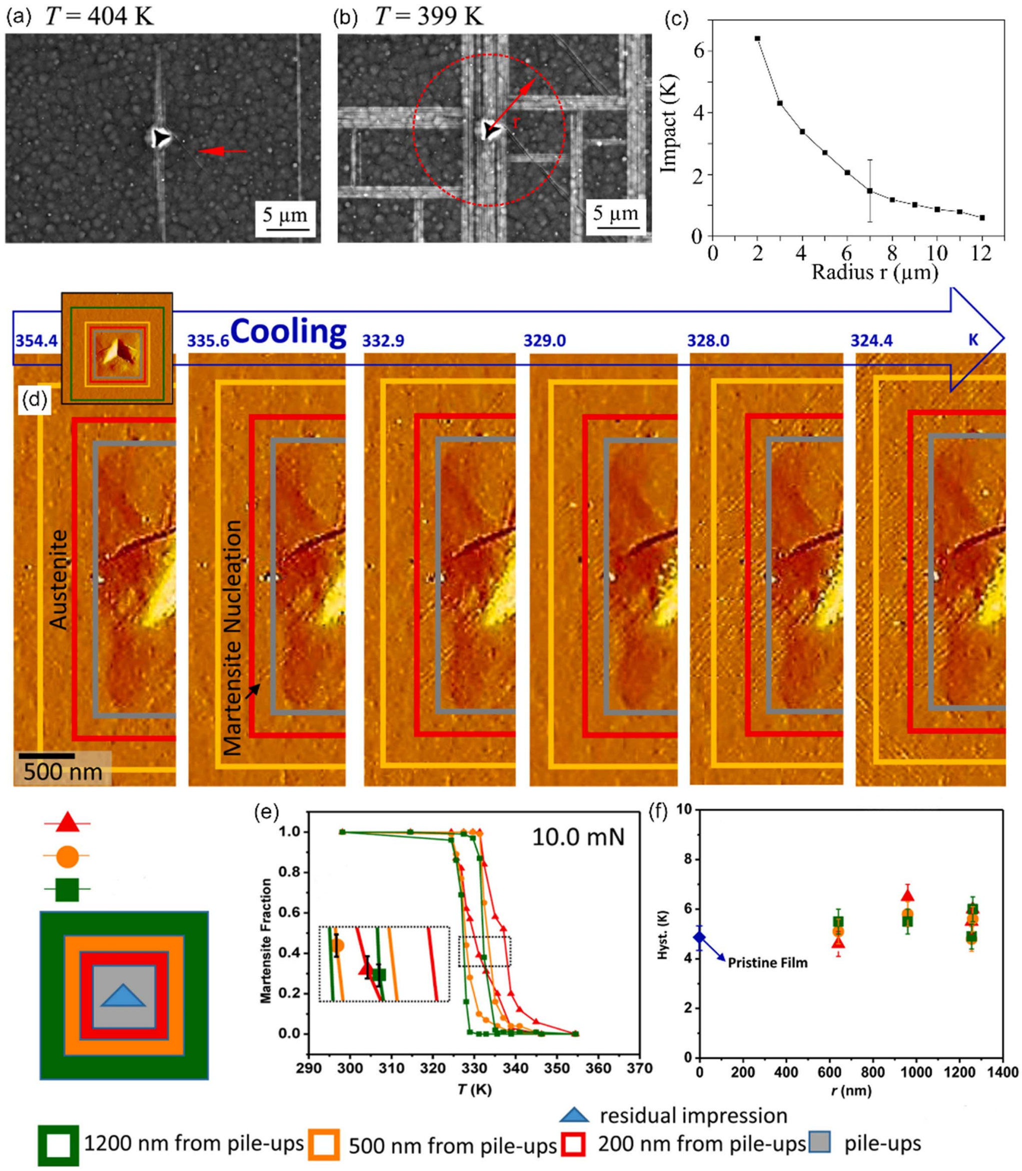

Figure 7. (a), (b) SEM images of the epitaxial $Ni_{48.4}Mn_{32.8}Ga_{18.8}$ film at different temperatures. (c) Dependency of the impact on the radius illustrated in (b). Reproduced from [79]. CC BY 4.0. (d) Morphology evolution of the epitaxial $Ni_{52.5}Mn_{20.7}Ga_{26.8}$ film as a function of temperature upon cooling. (e) Martensitic fraction as a function of temperature for the different zones around the indent. (f) Thermal hysteresis as a function of pile-up size for the different zones around the indent. Reprinted from [99], Copyright (2023), with permission from Elsevier.

(figures 13(f) and (g)). Such an exchange frustration leads to giant reversible magnetocaloric properties in the $GdCrTiO_5$ (figure 13(h)).

Atomic ordering also has a strong effect on the MCE [111–115]. Sánchez-Alarcos *et al* [113] investigated the influence of atomic ordering on the MCE in Ni–Co–Mn–In alloys. The atomic ordering in the Ni–Co–Mn–In alloys was adjusted by varying the quench temperature (T_{quench}). The martensitic transformation temperature shows a non-monotonous dependence on the T_{quench}, which displays opposite trends above and below 900 K, respectively (figure 14(a)). Such anomalous behavior can be attributed to a change in the degree of $L2_1$ atomic order (figure 14(b)). The magnetic exchange coupling in the austenite is sensitive to the atomic ordering, resulting in a variation in the magnetic contribution to the total entropy change [114]. Besides that, post-quench aging has proven to be an effective way to tune the transformation entropy since it tailors the long-range atomic ordering of austenite (figure 14(c)). The relationship between long-range atomic ordering and point defect was investigated in Ni–Co–Mn–Sn by Bruno *et al* [115]. The $L2_1$ ordering decreases with an increase in the point defect concentration. Therefore, rapidly quenched samples show lower $L2_1$ ordering than furnace cooled samples (figure 14(e)). The $L2_1$ ordering can be optimized by introducing a secondary heat treatment, which can lead to smaller thermal hysteresis, narrower transition width and higher RCP in the Ni–Mn–Co–Sn alloys (figures 14(f)–(g)) [115].

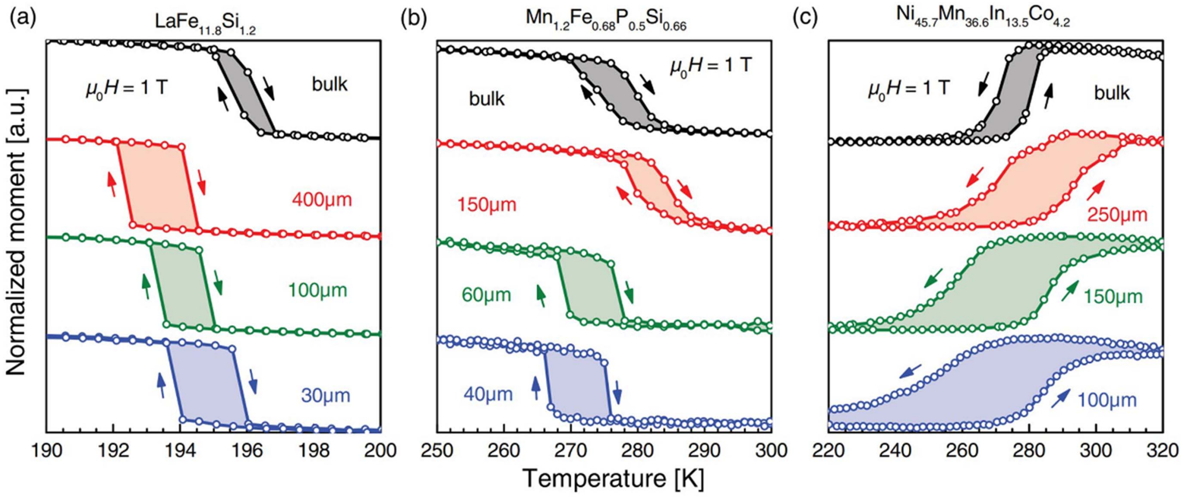

Figure 8. *M–T* curves of (a) $LaFe_{11.8}Si_{1.2}$, (b) $Mn_{1.2}Fe_{0.68}P_{0.5}Si_{0.66}$, and (c) $Ni_{45.7}Mn_{36.6}In_{13.5}Co_{4.2}$ with different particle size. [84] John Wiley & Sons. (Copyright © 2017 WILEY-VCH Verlag GmbH & Co. KGaA, Weinheim).

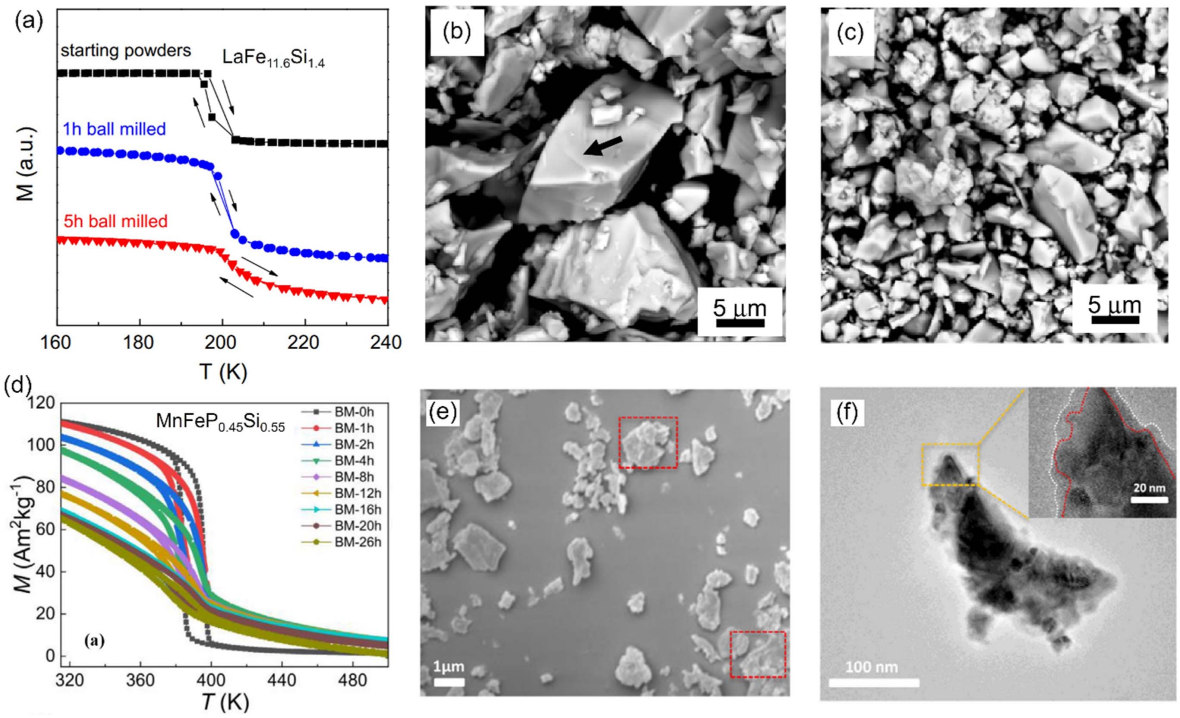

Figure 9. (a) *M–T* curves of $LaFe_{11.6}Si_{1.4}$ particles after different ball-milling times. SEM images of $LaFe_{11.6}Si_{1.4}$ particles after (b) 1 h ball milling and (c) 5 h ball milling. Reprinted from [80], Copyright (2012), with permission from Elsevier. (d) *M–T* curves for $MnFeP_{0.45}Si_{0.55}$ particles after different ball-milling time. (e) SEM image of $MnFeP_{0.45}Si_{0.55}$ particles after 16 h ball milling. (f) Bright-field TEM image of one particle after 26 h ball milling. Reproduced from [100]. CC BY 4.0.

2.6. Composites

Transition metal-based MCMs commonly have intrinsic brittleness and low thermal conductivity, which significantly hinder their practical applications [51]. To address this problem, the construction of magnetocaloric composites is an effective way to overcome these shortcomings. The most straightforward way to fabricate magnetocaloric composites is to bond the magnetocaloric powders with polymers [43, 63, 65–67] or low-melting point metals [62, 64, 68–76]. Figure 15(a) displays the typical microstructure of epoxy-bonded magnetocaloric composites, which were fabricated by mold pressing a mixture of $Mn_{0.98}CoGe$ particles and epoxy resin. The compressive stress of the $Mn_{0.98}CoGe$/epoxy composite with ∼5 wt.% epoxy is remarkably increased by about 360% compared to the $Mn_{0.98}CoGe$ bulk sample (figure 15(b)). However, the introduction of the non-magnetic epoxy causes degradation

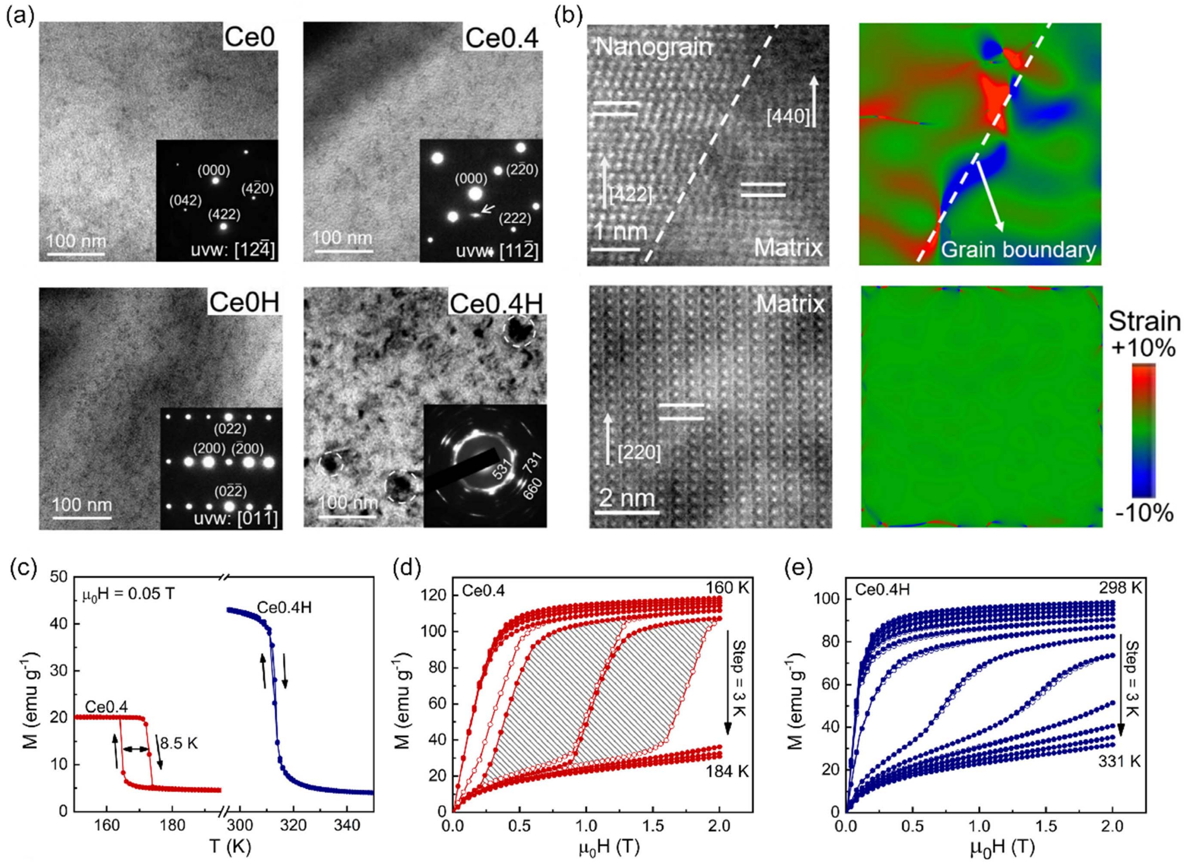

Figure 10. (a) Bright-field TEM images of the $La_{1-x}Ce_xFe_{11}Si_2$ samples and their hydrides. (b) High-resolution TEM images and the corresponding strain map near the nano-grain/matrix boundary in the $La_{0.6}Ce_{0.4}Fe_{11}Si_2H$ sample. (c) *M–T* curves of the $La_{0.6}Ce_{0.4}Fe_{11}Si_2$ samples before and after hydrogenation. The isothermal *M–H* curves for the $La_{0.6}Ce_{0.4}Fe_{11}Si_2$ samples (d) before and (e) after hydrogenation. Reprinted from [101], Copyright (2021), with permission from Elsevier.

of the magnetocaloric properties (figure 15(c)). Additionally, polymer-based binders usually possess low thermal conductivity ($\lambda < 1$ Wm^{-1} K^{-1}), which is detrimental to the heat exchange efficiency of the whole magnetocaloric composite.

Alternatively, the fabrication of magnetocaloric composites with metal-based binders is expected to realize both good mechanical stability and high thermal conductivity. Figure 15(d) shows the SEM image of the La–Fe–Si–H/Al composites, where the La–Fe–Si–H magnetocaloric particles are dispersedly distributed in the Al matrix [116]. Due to the high thermal conductivity of the Al matrix ($\lambda = 235$ Wm^{-1} K^{-1}), the La–Fe–Si/Al composites possess a high λ of 45.6 Wm^{-1} K^{-1} (figure 15(e)). However, the magnetocaloric performance is once again reduced due to the presence of 20 wt.% non-magnetic Al (figure 15(f)). Magnetocaloric composites do not necessarily have to be produced by bonding the magnetocaloric particles with polymer- or metal-based binders. A dual-phase microstructure may be directly formed during the solidification process from the molten state [117]. The design of non-stoichiometric La–Fe–Si MCMs with excess Fe leads to the formation of La–Fe–Si/α-Fe composites (figure 15(g)) [44]. The mechanical integrity is remarkably enhanced due to the presence of the soft α-Fe secondary phase that can withstand the stress and impede the propagation of cracks (figure 15(h)). Additionally, the giant MCE is preserved in the La–Fe–Si/α-Fe composites (figure 15(i)).

Based on finite-element simulations, Miao *et al* [76] pointed out that the spatial distribution of the secondary phase as well as the interfacial conditions between the secondary phase and magnetocaloric matrix strongly affect the thermal conductivity of the composites. A continuous distribution of secondary phase and coherent interfaces is highly desirable for greatly improving the thermal conductivity of magnetocaloric composites. They have successfully fabricated Mn–Fe–P–Si/Cu composites where continuous Cu networks are formed in the Mn–Fe–P–Si matrix (figures 16(a) and (b)). This novel microstructure was realized by hot pressing the Mn–Fe–P–Si/Cu core/shell powder that was synthesized by electroless Cu plating [76]. Besides, TEM analyses indicate the formation of dense and coherent interfaces between the Mn–Fe–P–Si matrix and Cu binder, which is beneficial for reducing the interfacial thermal resistance (figures 16(c)–(e)). As a result, the thermal conductivity and compressive strength are greatly enhanced by a factor of about 5 as compared to conventional bulk samples, while the magnetocaloric properties are slightly reduced due to the introduction of the non-magnetic Cu binder (figures 16(f)–(h)).

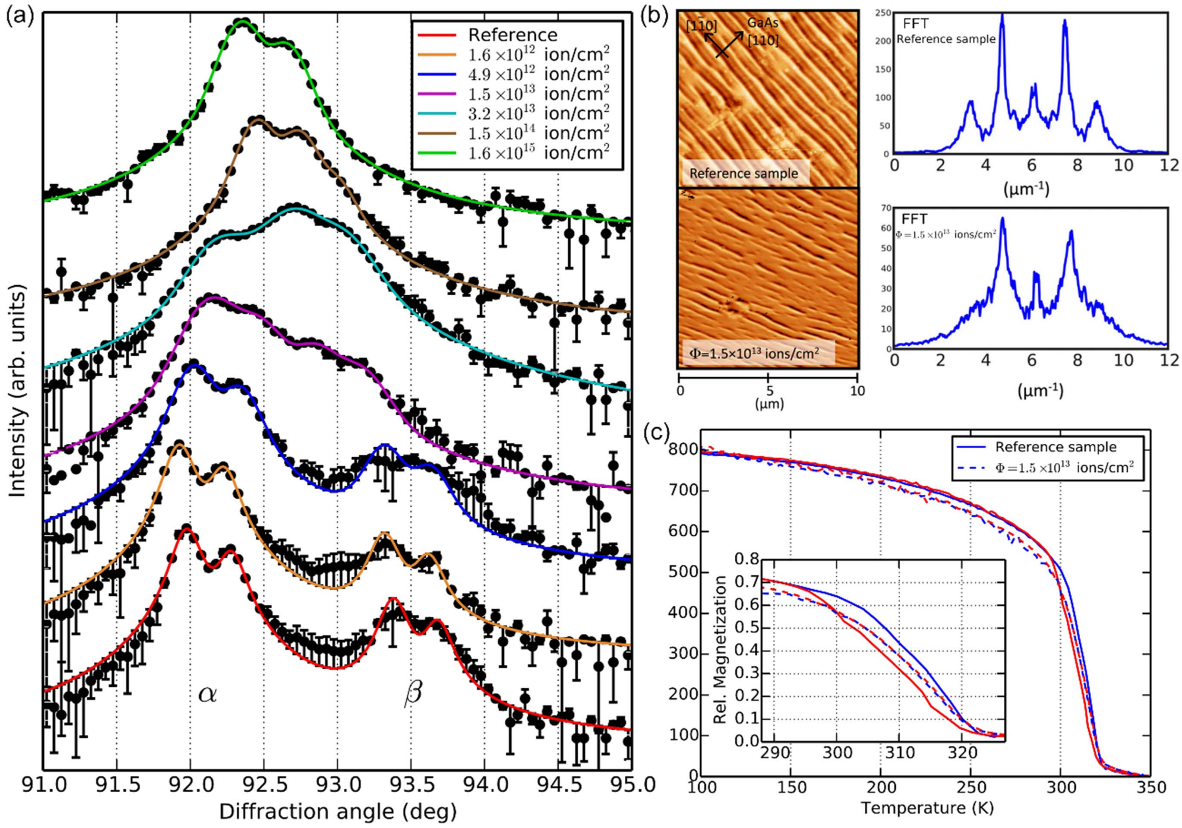

Figure 11. (a) XRD patterns, (b) MFM images, and (c) M–T curves of the MnAs films before and after ion irradiation. Reprinted from [103], with the permission of AIP Publishing.

3. Summary and outlook

In order to compete with conventional vapor-compression based refrigeration, magnetic refrigeration needs to overcome many challenges. MCMs, which are responsible for the actual cooling in a magnetic refrigerator, are expected to possess multiple outstanding properties. Beyond excellent magnetocaloric performance, they must present mechanical stability, good thermal conductivity, corrosion resistance and etc.

It is no coincidence that all materials considered promising for application present first order phase transitions. First order phase transitions concentrate the entropy and temperature changes in a narrow temperature interval due to the discontinuity of the entropy itself as a first order derivative of the Gibbs free energy. This results in excellent magnetocaloric performance. However, the energy barrier at the phase transition gives rise to thermal and field hysteresis which hinder reversibility immensely. Moreover, mechanical stability is an issue because of the discontinuity on the other first order derivative of the Gibbs free energy: volume. Fortunately, volume change and hysteresis behave synergistically and if you can decrease one the other follows suit. This is the case of Heusler alloys and Fe_2P-based compounds. On the former hysteresis can be decreased by increasing the geometrical compatibility between the phases at either side of the transition, while in the latter it can be decreased by tuning the phase transition to occur as close to the tricritical point as possible. These are ways of intrinsically reducing hysteresis. However, one can also extrinsically reduce hysteresis by engineering the microstructure of the material. This can be done by introducing defects where nucleation can start more easily or by creating strong textures which lower the mismatch between neighboring grains decreasing the strain accumulation due to the phase change. Of all techniques presented in this paper that achieve the latter perhaps the simplest is also the most powerful and promising. Magnetic field alignment is a simple and elegant technique which can be implemented at low cost and gives the chance of using a binder that further improves mechanical stability and boosts thermal conductivity within the material itself, as was recently demonstrated by Zhou *et al* [87] and Guo *et al* [91]. It also taps into the so-called size effect since it allows control of the grain size as well.

In this sense, techniques which combine different approaches are also the ones which show the most promise to improve thermal conductivity. The fabrication of composites using electroless plating combines size effect and a high thermal conductivity binder. The results are incredibly promising. On one hand, the formation of a honeycomb Cu network dramatically improves thermal conductivity. On the other, the combination of a ductile binder and the geometrical compatibility between matrix and binder boosted mechanical stability in Fe_2P-based materials.

Overall, this article provides an overview of different microstructural manipulation strategies utilized to

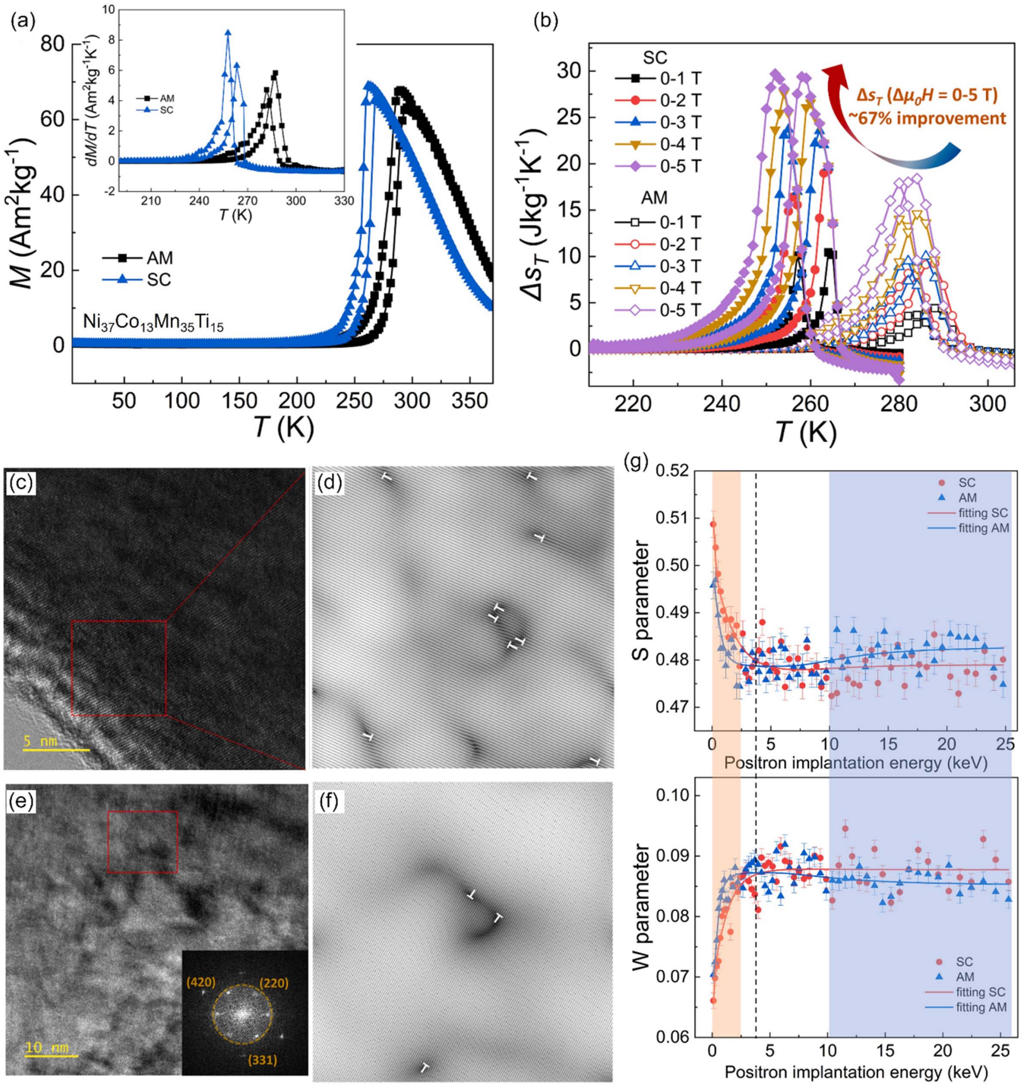

Figure 12. (a) M–T and (b) ΔS–T curves for the AM and SC samples. TEM results of (c), (d) the AM and (e), (f) SC samples. (g) S and W parameters versus the position implantation energy for the AM and SC samples derived from PAS measurements. Reproduced from [81].

improve the comprehensive properties of MCMs, which are complementary to the commonly used compositional optimization approach. The key message is that the various microstructural manipulation strategies can be extended beyond transition metal-based MCMs and also inspire the development of new solutions. This, we expect, will accelerate the commercialization of magnetic refrigeration and magnetocaloric power regeneration.

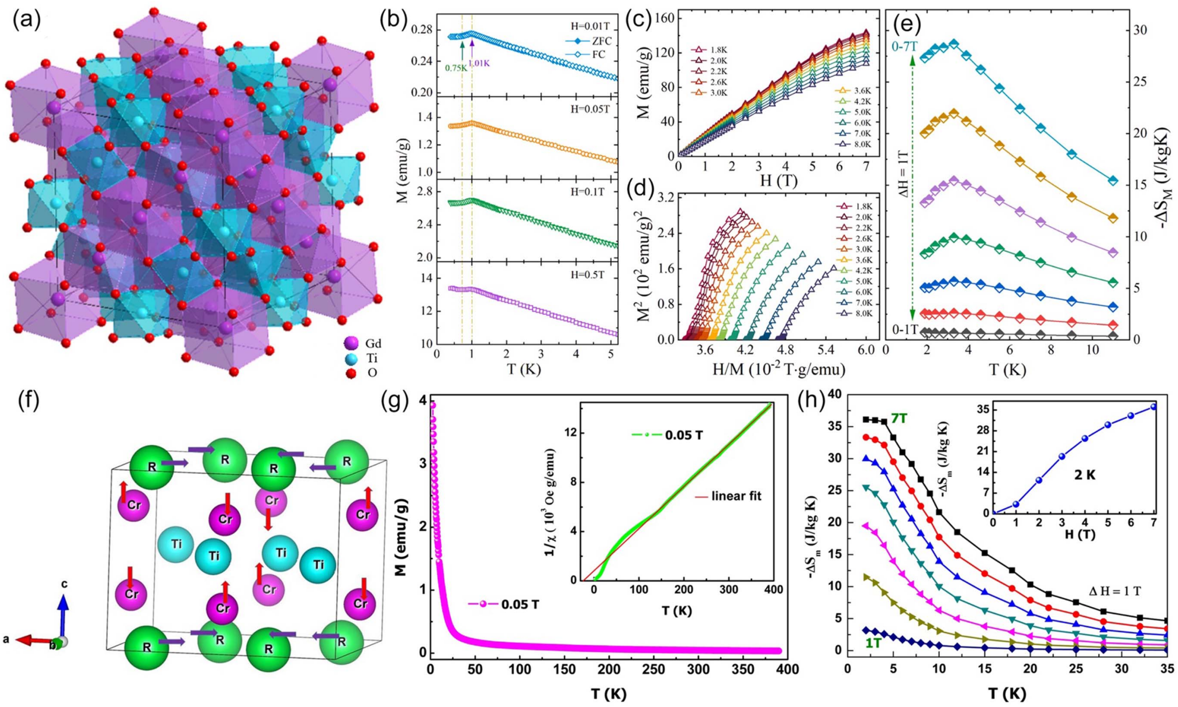

Figure 13. (a) Crystal structure, (b) M–T curves, (c) M–H curves, (d) Arrot plots, and (e) ΔS–T curves of the $Gd_2Ti_2O_7$ oxide. Reprinted from [106], Copyright (2024), with permission from Elsevier. (f) Crystal and magnetic structure, (g) M–T curve, and (h) ΔS–T curves of the $GdCrTiO_5$ oxide. Reprinted (figure) with permission from [107], Copyright (2018) by the American Physical Society.

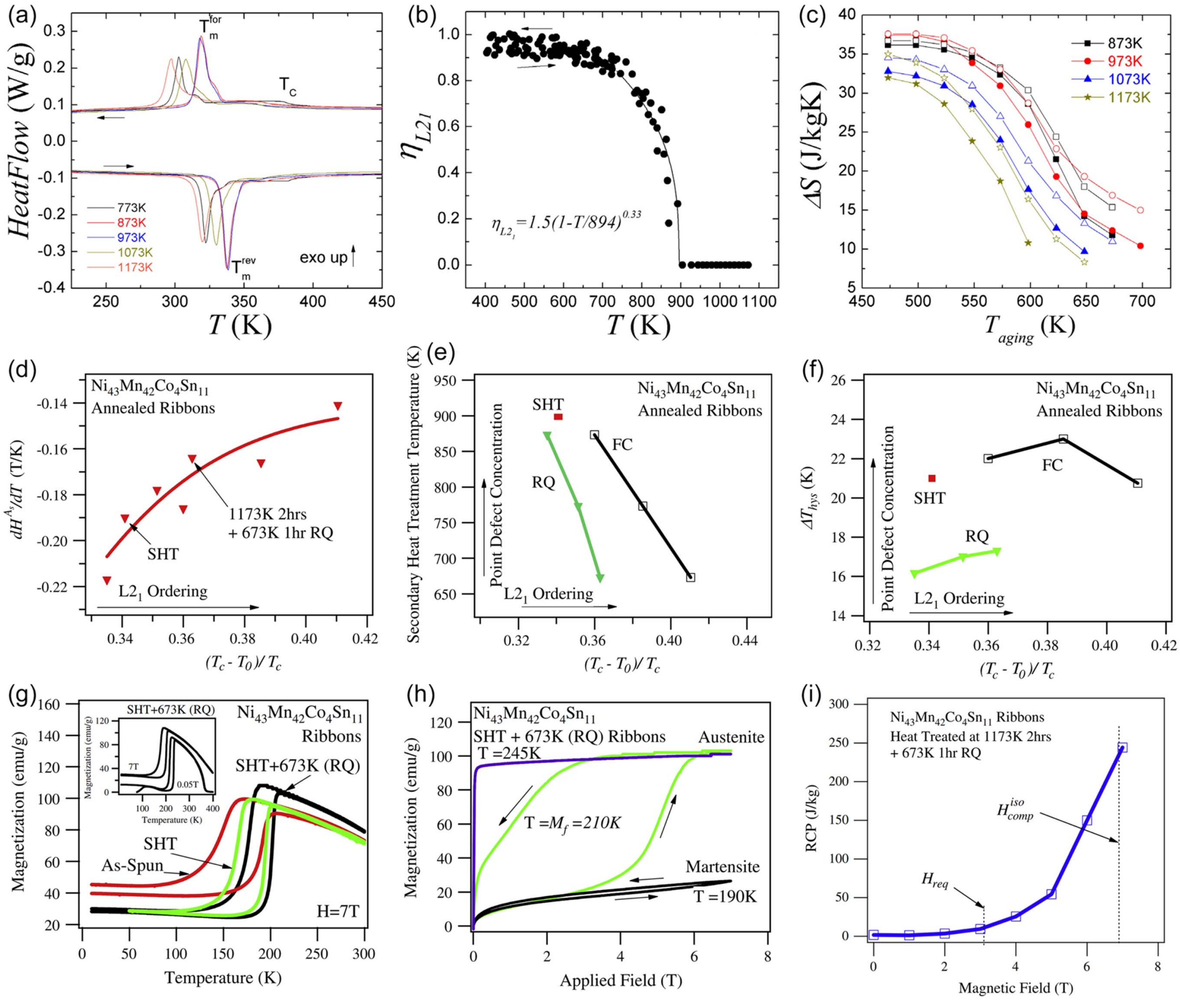

Figure 14. (a) DSC curves of the Ni–Mn–Sn–Co samples with different quenching temperatures. (b) Temperature dependence of the $L2_1$ order parameter. (c) Transformation entropy after different post-quenching ageing. Reproduced from [113]. CC BY 4.0. (d) Field sensitivity of the transformation temperature, (e) secondary heat treatment temperature, and (f) ΔT_{hys} as a function of $(T_C–T_0)/T_C$ for secondary heat-treated $Ni_{43}Mn_{42}Co_4Sn_{11}$ samples. (g) $M–T$ curves, (h) $M–H$ curves, and (i) RCP under different applied fields of the secondary heat-treated samples. Reprinted from [115], Copyright (2014), with permission from Elsevier.

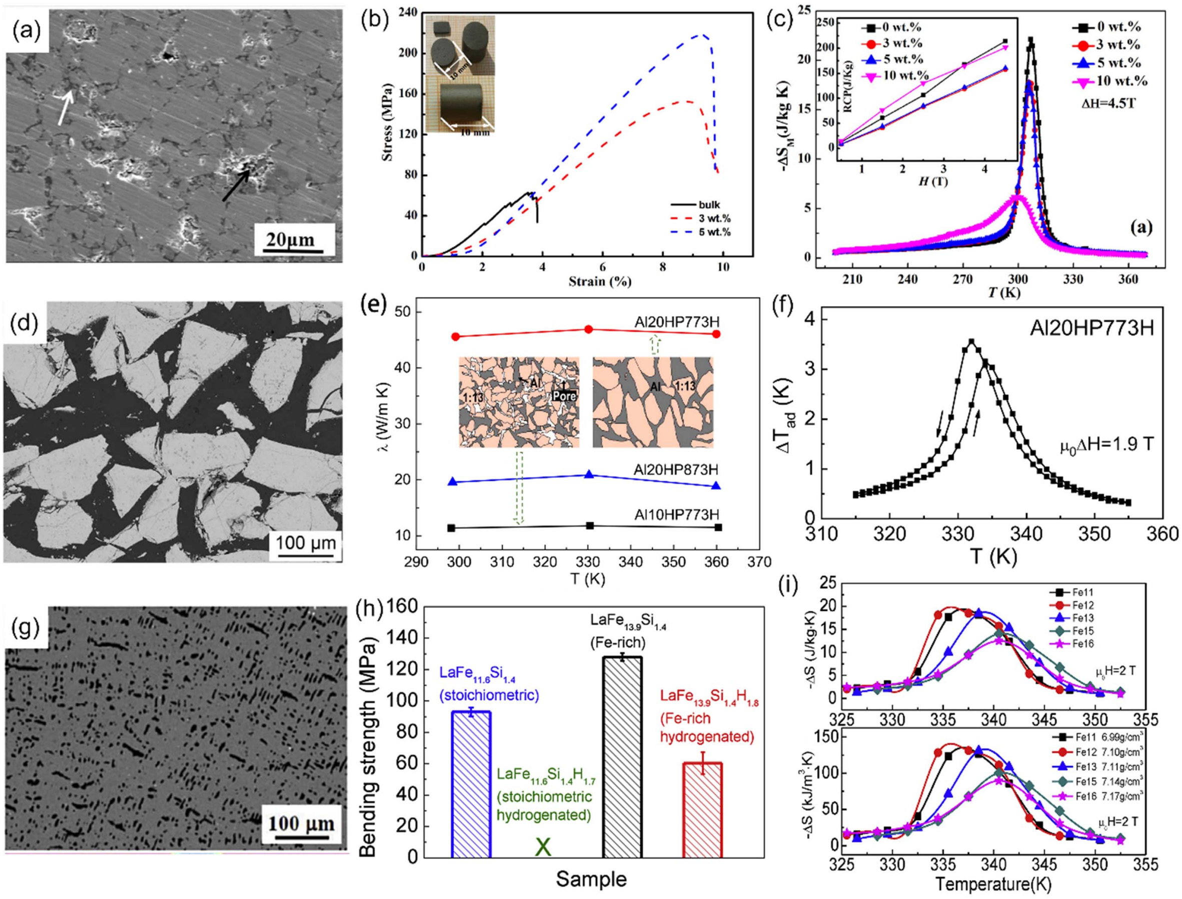

Figure 15. (a) SEM image, (b) compressive stress–strain curves, and (c) isothermal entropy change of $Mn_{0.98}CoGe$/epoxy composite. Reprinted from [65], Copyright (2018), with permission from Elsevier. (d) SEM image, (e) thermal conductivity, and (f) adiabatic temperature change of La–Fe–Si/Al composite. Reprinted from [116], Copyright (2023), with permission from Elsevier. (g) SEM image, (h) bending stress, and (i) mass and volumetric total entropy change of La–Fe–Si/α-Fe composites. Reprinted from [44], Copyright (2017), with permission from Elsevier.

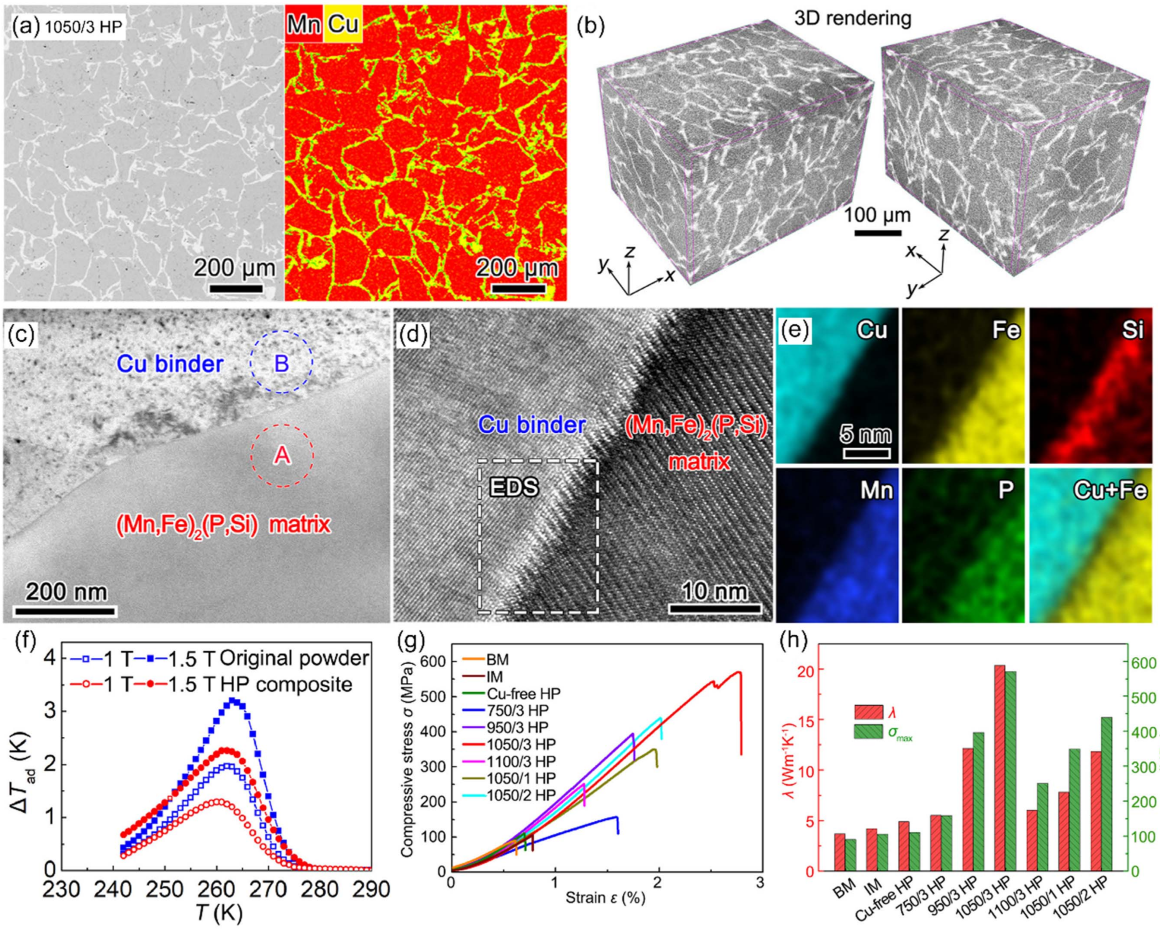

Figure 16. (a) SEM image and corresponding EDS maps, (b) 3D-CT images, (c)–(e) TEM analyses, (f) adiabatic temperature change, (g) compressive stress–strain curves, and (h) thermal conductivity of the Mn–Fe–P–Si/Cu network composites. Reprinted from [76], Copyright (2023), with permission from Elsevier.

Data availability statement

All data that support the findings of this study are included within the article (and any supplementary files).

Acknowledgments

This work was supported by the National Natural Science Foundation of China [Grant Numbers, U1832191, 52001167; 52371189]; the Natural Science Foundation of Jiangsu Province (Grant Number BK20231458); the Sino-German Mobility Program from the Sino-German Center for Research Promotion (SGC) [Grant Numbers M-0447]. This work was carried out in the framework of the Joint Lab BiBer.

ORCID iDs

Yong Gong https://orcid.org/0009-0005-7850-9311
Xuefei Miao https://orcid.org/0000-0003-4930-9108
Feng Xu https://orcid.org/0000-0001-5802-7925
Luana Caron https://orcid.org/0000-0002-2291-9814

References

[1] Salehy Y, Hoang H M, Cluzel F, Leroy Y, Delahaye A, Fournaison L and Yannou B 2020 Energy performances assessment for sustainable design recommendations: case study of a supermarket's refrigeration system *Proc. CIRP* **90** 328–33

[2] Llopis R, Sánchez D and Cabello R 2017 Refrigerants for vapor compression refrigeration systems: a review on natural and artificial heat transfer fluids *Advances in New Heat Transfer Fluids: From Numerical to Experimental Techniques*, ed A A Minea (CRC Press) pp 463–522

[3] Belman-Flores J M, Barroso-Maldonado J M, Rodríguez-Muñoz A P and Camacho-Vázquez G 2015 Enhancements in domestic refrigeration, approaching a sustainable refrigerator—a review *Renew. Sustain. Energy Rev.* **51** 955–68

[4] Chaudhary V, Chen X and Ramanujan R V 2019 Iron and manganese based magnetocaloric materials for near room temperature thermal management *Prog. Mater. Sci.* **100** 64–98

[5] Moya X and Mathur N 2020 Caloric materials for cooling and heating *Science* **370** 797–803

[6] Franco V, Blázquez J S, Ingale B and Conde A 2012 The magnetocaloric effect and magnetic refrigeration near room temperature: materials and models *Annu. Rev. Mater. Res.* **42** 305–42

[7] Srivastava B K, Eriksson T, Haggstrom L, Verma H R, Andersson Y and Rundqvist S 1987 A Mossbauer study of the $(Fe_{1-x}Mn_x)_2P$ system *J. Phys. C: Solid State Phys.* **20** 10

[8] Kitanovski A 2020 Energy applications of magnetocaloric materials *Adv. Energy Mater.* **10** 1903741

[9] Balli M, Jandl S, Fournier P and Kedous-Lebouc A 2017 Advanced materials for magnetic cooling: fundamentals and practical aspects *Appl. Phys. Rev.* **4** 021305

[10] Liu X *et al* 2023 High-performance thermomagnetic generator controlled by a magnetocaloric switch *Nat. Commun.* **14** 4811

[11] Tishin A M, Spichkin Y I, Zverev V I and Egolf P W 2016 A review and new perspectives for the magnetocaloric effect: new materials and local heating and cooling inside the human body *Int. J. Refrig.* **68** 177–86

[12] Romero-Muñiz C, Law J Y, Revuelta-Losada J, Moreno-Ramírez L M and Franco V 2023 Magnetocaloric materials for hydrogen liquefaction *Innov. Mater.* **1** 100045

[13] Liu J 2023 Choosing a cool magnetic material for H_2 liquification *Innov. Mater.* **1** 100031

[14] Tang X *et al* 2022 Magnetic refrigeration material operating at a full temperature range required for hydrogen liquefaction *Nat. Commun.* **13** 1817

[15] Zhang H, Gimaev R, Kovalev B, Kamilov K, Zverev V and Tishin A 2019 Review on the materials and devices for magnetic refrigeration in the temperature range of nitrogen and hydrogen liquefaction *Physica* B **558** 65–73

[16] Dzekan D, Waske A, Nielsch K and Fähler S 2021 Efficient and affordable thermomagnetic materials for harvesting low grade waste heat *APL Mater.* **9** 011105

[17] Kishore R A and Priya S 2018 A review on design and performance of thermomagnetic devices *Renew. Sustain. Energy Rev.* **81** 33–44

[18] Greco A, Aprea C, Maiorino A and Masselli C 2019 A review of the state of the art of solid-state caloric cooling processes at room-temperature before 2019 *Int. J. Refrig.* **106** 66–88

[19] Zimm C, Boeder A, Mueller B, Rule K and Russek S L 2018 The evolution of magnetocaloric heat-pump devices *MRS Bull.* **43** 274–9

[20] Kitanovski A, Tušek J, Tomc U, Plaznik U, Ozbolt M and Poredoš A 2015 *Magnetocaloric Energy Conversion: From Theory to Applications* (Springer)

[21] Zhang F, Miao X, van Dijk N, Brück E and Ren Y 2024 Advanced magnetocaloric materials for energy conversion: recent progress, opportunities, and perspective *Adv. Energy Mater.* **14** 2400369

[22] Hou H, Qian S and Takeuchi I 2022 Materials, physics and systems for multicaloric cooling *Nat. Rev. Mater.* **7** 633–52

[23] Law J Y, Franco V, Moreno-Ramírez L M, Conde A, Karpenkov D Y, Radulov I, Skokov K P and Gutfleisch O 2018 A quantitative criterion for determining the order of magnetic phase transitions using the magnetocaloric effect *Nat. Commun.* **9** 2680

[24] Xiang J *et al* 2024 Giant magnetocaloric effect in spin supersolid candidate $Na_2BaCo(PO_4)_2$ *Nature* **625** 270–5

[25] Gottschall T, Gràcia-Condal A, Fries M, Taubel A, Pfeuffer L, Mañosa L, Planes A, Skokov K P and Gutfleisch O 2018 A multicaloric cooling cycle that exploits thermal hysteresis *Nat. Mater.* **11** 620–6

[26] Franco V, Blázquez J S, Ipus J J, Law J Y, Moreno-Ramírez L M and Conde A 2018 Magnetocaloric effect: from materials research to refrigeration devices *Prog. Mater. Sci.* **93** 112–232

[27] Wojcieszak S, Wodajo B, Duong A, Hadimani R and Barua R 2022 A brief review on the chemical stability and corrosivity of magnetocaloric materials *JOM* **74** 4368–78

[28] Tegus O, Brück E, Buschow K H J and de Boer F R 2002 Transition-metal-based magnetic refrigerants for room-temperature applications *Nature* **415** 150–2

[29] Guillou F, Porcari G, Yibole H, van Dijk N H and Brück E 2014 Taming the first-order transition in giant magnetocaloric materials *Adv. Mater.* **26** 2671

[30] Hu F X, Shen B G, Sun J R, Cheng Z H, Rao G H and Zhang X X 2001 Influence of negative lattice expansion and metamagnetic transition on magnetic entropy change in the compound $LaFe_{11.4}Si_{1.6}$ *Appl. Phys. Lett.* **78** 3675–7

[31] Fujieda S, Fujita A and Fukamichi K 2002 Large magnetocaloric effect in $La(Fe_xSi_{1-x})_{13}$ itinerant-electron metamagnetic compounds *Appl. Phys. Lett.* **81** 1276

[32] Trung N T, Zhang L, Caron L, Buschow K H J and Brück E 2010 Giant magnetocaloric effects by tailoring the phase transitions *Appl. Phys. Lett.* **96** 172504

[33] Shen F *et al* 2020 Cone-spiral magnetic ordering dominated lattice distortion and giant negative thermal expansion in Fe-doped MnNiGe compounds *Mater. Horiz.* **7** 804–10

[34] Krenke T, Duman E, Acet M, Wassermann E F, Moya X, Manosa L and Planes A 2005 Inverse magnetocaloric effect in ferromagnetic Ni-Mn-Sn alloys *Nat. Mater.* **4** 450–4

[35] Liu J, Gottschall T, Skokov K P, Moore J D and Gutfleisch O 2012 Giant magnetocaloric effect driven by structural transitions *Nat. Mater.* **11** 620–6

[36] Wei Z Y *et al* 2016 Magnetostructural martensitic transformations with large volume changes and magneto-strains in all-d-metal Heusler alloys *Appl. Phys. Lett.* **109** 071904

[37] Boeije M F J, Roy P, Guillou F, Yibole H, Miao X F, Caron L, Banerjee D, van Dijk N H, de Groot R A and Brück E 2016 Efficient room-temperature cooling with magnets *Chem. Mater.* **28** 4901–5

[38] Miao X *et al* 2020 Switching the magnetostructural coupling in MnCoGe-based magnetocaloric materials *Phys. Rev. Mater.* **4** 104407

[39] Scheibel F *et al* 2018 Hysteresis design of magnetocaloric materials-from basic mechanisms to applications *Energy Technol.* **6** 1397–428

[40] Law J Y and Franco V 2022 Review on magnetocaloric high-entropy alloys: design and analysis methods *J. Mater. Res.* **38** 37–51

[41] Law J Y, Moreno-Ramírez L M, Díaz-García Á and Franco V 2023 Current perspective in magnetocaloric materials research *J. Appl. Phys.* **133** 040903

[42] Kuz'min M D 2007 Factors limiting the operation frequency of magnetic refrigerators *Appl. Phys. Lett.* **90** 251916

[43] Skokov K P, Karpenkov D Y, Kuz'min M D, Radulov I A, Gottschall T, Kaeswurm B, Fries M and Gutfleisch O 2014 Heat exchangers made of polymer-bonded La(Fe,Si)$_{13}$ *J. Appl. Phys.* **115** 17A941

[44] Shao Y, Liu J, Zhang M, Yan A, Skokov K P, Karpenkov D Y and Gutfleisch O 2017 High-performance solid-state cooling materials: balancing magnetocaloric and non-magnetic properties in dual phase La-Fe-Si *Acta Mater.* **125** 506–12

[45] Funk A, Zeilinger M, Miehe A, Sopu D, Eckert J, Dötz F and Waske A 2018 MnFePSi-based magnetocaloric packed bed regenerators: structural details probed by x-ray tomography *Chem. Eng. Sci.* **175** 84–90

[46] Wang C, Miao X, Zha J, Guo W, Ren Q, Zhang Y, Xu F and Caron L 2023 Novel fabrication of honeycomb-like magnetocaloric regenerators via a self-organization process *Scr. Mater.* **223** 115067

[47] Sun W, Zhang M, Fu Q, Li Z, Mo Z and Li G 2023 Opportunities and challenges of additive manufacturing toward magnetic refrigeration *Innov. Mater.* **1** 100032

[48] Lu X, Miao L, Zhang Y, Wang Z, Zhang H, Li G and Liu J 2023 First-order phase transition La-Fe-Si bulk materials with small hysteresis by laser powder bed fusion: microstructure and magnetocaloric effect *Scr. Mater.* **232** 115479

[49] Maiorino A, Del Duca M G, Tomc U, Tušek J, Kitanovski A and Aprea C 2021 A numerical modelling of a multi-layer LaFeCoSi active magnetic regenerator by using artificial neural networks *Appl. Therm. Eng.* **197** 117375

[50] Turcaud J A, Bez H N, Ruiz-Trejo E, Bahl C R H, Nielsen K K, Smith A and Cohen L F 2015 Influence of manganite powder grain size and Ag-particle coating on the magnetocaloric effect and the active magnetic regenerator performance *Acta Mater.* **97** 413–8

[51] Gottschall T, Skokov K P, Fries M, Taubel A, Radulov I, Scheibel F, Benke D, Riegg S and Gutfleisch O 2019 Making a cool choice: the materials library of magnetic refrigeration *Adv. Energy Mater.* **9** 1901322

[52] Qu Y H, Cong D Y, Li S H, Gui W Y, Nie Z H, Zhang M H, Ren Y and Wang Y D 2018 Simultaneously achieved large reversible elastocaloric and magnetocaloric effects and their coupling in a magnetic shape memory alloy *Acta Mater.* **151** 41–55

[53] Taake C, Samanta T and Caron L 2024 Field-sensitivity and reversibility of the inverse magnetocaloric effect at martensitic transformations *Appl. Phys. Lett.* **124** 052403

[54] Yang J, Li Z, Zhang X, Yang B, Yan H, Cong D, Zhao X and Zuo L 2023 Manipulation of thermal hysteresis and magnetocaloric effect in the Ni-Co-Mn-In alloys through lattice contraction: effect of Ge substitution for In *Acta Mater.* **246** 118694

[55] Qu Y, Sun X, Gui W, Li R, Nie Z, Gao Z, Cai W, Ren Y, Wang Y and Cong D 2023 Complete and reversible magnetostructural transition driven by low magnetic field in multiferroic NiCoMnIn alloys *Acta Mater.* **243** 118535

[56] Liu J, Gong Y, You Y, You X, Huang B, Miao X, Xu G, Xu F and Brück E 2019 Giant reversible magnetocaloric effect in MnNiGe-based materials: minimizing thermal hysteresis via crystallographic compatibility modulation *Acta Mater.* **174** 450–8

[57] Zhang G, Li D, Liu C, Li Z, Yang B, Yan H, Zhao X and Zuo L 2021 Giant low-field actuated caloric effects in a textured $Ni_{43}Mn_{47}Sn_{10}$ alloy *Scr. Mater.* **201** 113947

[58] Li Z, Li Z, Yang B, Zhao X and Zuo L 2018 Giant low-field magnetocaloric effect in a textured $Ni_{45.3}Co_{5.1}Mn_{36.1}In_{13.5}$ alloy *Scr. Mater.* **151** 61–65

[59] Zhang H, Zhang X, Qian M, Yao Z, Wei L and Geng L 2020 Increasing working temperature span in Ni-Mn-Sn-Co alloys via introducing pores *J. Magn. Magn. Mater.* **500** 166359

[60] Cavazzini G *et al* 2022 Effect of size and disorder on martensitic phase transition and thermal hysteresis in milled Ni-Mn-In-Co microparticles *J. Alloys Compd.* **906** 164377

[61] Zhang Z *et al* 2020 Self-organized Bi-rich grain boundary precipitates for realizing steep magnetic-field-driven metamagnetic transition in Bi-doped Mn_2Sb *Acta Mater.* **200** 835–47

[62] Wang Y, Zhang H, Liu E, Zhong X, Tao K, Wu M, Xing C, Xiao Y, Liu J and Long Y 2018 Outstanding comprehensive performance of La(Fe,Si)$_{13}$H$_y$/In composite with durable service life for magnetic refrigeration *Adv. Electron. Mater.* **4** 1700636

[63] Coppi C, Cugini F, Magnani G, Milanese C, Nasi L, Lazzarini L, Pontiroli D, Riccò M and Solzi M 2022 Graphene-based magnetocaloric composites for energy conversion *Adv. Eng. Mater.* **25** 2200811

[64] Radulov I A, Karpenkov D Y, Skokov K P, Karpenkov A Y, Braun T, Brabänder V, Gottschall T, Pabst M, Stoll B and Gutfleisch O 2017 Production and properties of metal-bonded La(Fe,Mn,Si)$_{13}$H$_x$ composite material *Acta Mater.* **127** 389–99

[65] Zhu F, Lin J C, Jiang W B, Yang C, Li L F, Zhang X K, Song W H, Zhu X B, Tong P and Sun Y P 2018 Enhanced mechanical properties and large magnetocaloric effects in epoxy-bonded $Mn_{0.98}CoGe$ *Scr. Mater.* **150** 96–100

[66] Pulko B *et al* 2015 Epoxy-bonded La-Fe-Co-Si magnetocaloric plates *J. Magn. Magn. Mater.* **375** 65–73

[67] Radulov I A, Skokov K P, Karpenkov D Y, Braun T and Gutfleisch O 2015 Polymer-bonded La(Fe,Mn,Si)$_{13}$H$_x$ plates for heat exchangers *IEEE Trans. Magn.* **51** 2501204

[68] Lyubina J, Hannemann U, Cohen L F and Ryan M P 2012 Novel La(Fe,Si)$_{13}$/Cu composites for magnetic cooling *Adv. Energy Mater.* **2** 1323–7
[69] Krautz M, Funk A, Skokov K P, Gottschall T, Eckert J, Gutfleisch O and Waske A 2015 A new type of La(Fe,Si)$_{13}$-based magnetocaloric composite with amorphous metallic matrix *Scr. Mater.* **95** 50–53
[70] Zhang H, Liu J, Zhang M, Shao Y, Li Y and Yan A 2016 $LaFe_{11.6}Si_{1.4}H_y$/Sn magnetocaloric composites by hot pressing *Scr. Mater.* **120** 58–61
[71] Dong X T, Zhong X C, Peng D R, Huang J H, Zhang H, Jiao D L, Liu Z W and Ramanujan R V 2018 $La_{0.8}Ce_{0.2}(Fe_{0.95}Co_{0.05})_{11.8}Si_{1.2}/Sn_{42}Bi_{58}$ magnetocaloric composites prepared by low temperature hot pressing *J. Alloys Compd.* **737** 568–74
[72] Ouyang Y, Zhang H, Zhang M, Liu J, Yu G and Liu Z 2019 Simultaneous achievement of enhanced thermal conductivity and large magnetic entropy change in La-Fe-Si-H/Sn composites by optimizing interface contacts and hot pressing parameters *J. Alloys Compd.* **804** 49–56
[73] Zhang M, Ouyang Y, Zhang Y and Liu J 2020 $LaFe_{11}Co_{0.8}Si_{1.2}$/Al magnetocaloric composites prepared by hot pressing *J. Alloys Compd.* **823** 153846
[74] Zhang Y C, Franco V, Peng H X and Qin F X 2021 Structure and magnetic study of Ni-Mn-Ga/Al composite with modified magnetocaloric properties and enhanced thermal conductivity *Scr. Mater.* **201** 113956
[75] Zhong X C *et al* 2021 Microstructural evolution, magnetocaloric effect, mechanical and thermal properties of hot-pressed $LaFe_{11.6}Si_{1.4}/Ce_2Co_7$ composites prepared using strip-cast master alloy flakes *J. Magn. Magn. Mater.* **525** 167652
[76] Miao X *et al* 2023 Novel magnetocaloric composites with outstanding thermal conductivity and mechanical properties boosted by continuous Cu network *Acta Mater.* **242** 118453
[77] Zhong S, Qian M, Zhang J, Zhang Q, Sun L, Shen P, Zhang X and Geng L 2024 Microstructure and magnetocaloric effect in nonequilibrium solidified Ni-Mn-Sn-Co alloy prepared by laser powder bed fusion *Addit. Manuf.* **79** 103941
[78] Liang L, Tong W, Wang H J and Peng L M 2023 Enhancing magnetocaloric properties of NiMnGa-based alloys via Dy micro-alloying and pseudoelastic cyclic training *Appl. Phys. Lett.* **123** 022409
[79] Niemann R, Hahn S, Diestel A, Backen A, Schultz L, Nielsch K, Wagner M F X and Fähler S 2016 Reducing the nucleation barrier in magnetocaloric Heusler alloys by nanoindentation *APL Mater.* **4** 064101
[80] Liu J, Moore J D, Skokov K P, Krautz M, Löwe K, Barcza A, Katter M and Gutfleisch O 2012 Exploring La(Fe,Si)$_{13}$-based magnetic refrigerants towards application *Scr. Mater.* **67** 584
[81] Zhang F *et al* 2024 Impact of fast-solidification on all-d-metal NiCoMnTi based giant magnetocaloric Heusler compounds *Acta Mater.* **265** 119595
[82] Cugini F, Porcari G, Fabbrici S, Albertini F and Solzi M 2016 Influence of the transition width on the magnetocaloric effect across the magnetostructural transition of Heusler alloys *Phil. Trans. R. Soc.* A **374** 20150306
[83] Shamberger P J and Ohuchi F S 2009 Hysteresis of the martensitic phase transition in magnetocaloric-effect Ni-Mn-Sn alloys *Phys. Rev.* B **79** 144407
[84] Gottschall T, Benke D, Fries M, Taubel A, Radulov I A, Skokov K P and Gutfleisch O 2017 A matter of size and stress: understanding the first-order transition in materials for solid-state refrigeration *Adv. Funct. Mater.* **27** 1606735
[85] Guo W *et al* 2024 Significantly enhanced reversibility and mechanical stability in grain-oriented MnNiGe-based smart materials *Acta Mater.* **263** 119530
[86] Gong Y *et al* 2024 Anomalous thermal expansion and enhanced magnetocaloric effect in <001>-textured $Mn_xFe_{5-x}Si_3$ alloys *Rare Met.* **43** 2263–74
[87] Zhou H, Tao K, Chen B, Chen H, Qiao K, Yu Z, Cong J, Huang R, Taskaev S V and Zhang H 2022 Low-melting metal bonded MM′X/In composite with largely enhanced mechanical property and anisotropic negative thermal expansion *Acta Mater.* **229** 117830
[88] Li D, Li Z, Zhang X, Yang B, Wang D, Zhao X and Zuo L 2020 Enhanced cyclability of elastocaloric effect in a directionally solidified $Ni_{55}Mn_{18}Ga_{26}Ti_1$ alloy with low hysteresis *Scr. Mater.* **189** 78–83
[89] Shen Y, Wei Z, Sun W, Zhang Y, Liu E and Liu J 2020 Large elastocaloric effect in directionally solidified all-d-metal Heusler metamagnetic shape memory alloys *Acta Mater.* **188** 677–85
[90] Imaizumi K, Fujita A, Suzuki A, Kobashi M and Kato M 2024 Additive manufacturing for 3D microchannel structure using $La(Fe_xSi_{1-x})_{13}$ magnetic refrigerant via laser powder bed fusion *Addit. Manuf.* **83** 104076
[91] Guo W, Miao X, Yan Z, Chen Y, Gong Y, Qian F, Xu F and Caron L 2024 Colossal negative thermal expansion over a wide temperature span in dynamically self-assembled MnCo(Ge,Si)/epoxy composites *Mater. Res. Lett.* **12** 315–23
[92] Wu Y, Wang J, Jiang C and Xu H 2018 Effect of coherent nanoprecipitates on martensitic transformation in Tb-doped NiMnGa melt-spun ribbons *Intermetallics* **97** 42–51
[93] Tong W, Liang L, Xu J, Wang H J, Tian J and Peng L M 2022 Achieving enhanced mechanical, pseudoelastic and elastocaloric properties in Ni-Mn-Ga alloys via Dy micro-alloying and isothermal mechanical cyclic training *Scr. Mater.* **209** 114393
[94] Sepehri-Amin H, Taubel A, Ohkubo T, Skokov K P, Gutfleisch O and Hono K 2018 Microstructural origin of hysteresis in Ni-Mn-In based magnetocaloric compounds *Acta Mater.* **147** 342–9
[95] Provenzano V, Shapiro A J and Shull R D 2004 Reduction of hysteresis losses in the magnetic refrigerant $Gd_5Ge_2Si_2$ by the addition of iron *Nature* **429** 853–7
[96] Lyubina J, Schafer R, Martin N, Schultz L and Gutfleisch O 2010 Novel design of La(Fe,Si)$_{13}$ alloys towards high magnetic refrigeration performance *Adv. Mater.* **22** 3735
[97] Monroe J A, Cruz-Perez J, Yegin C, Karaman I, Geltmacher A B, Everett R K and Kainuma R 2012 Magnetic response of porous NiCoMnSn metamagnetic shape memory alloys fabricated using solid-state replication *Scr. Mater.* **67** 116–9
[98] Backen A, Yeduru S R, Kohl M, Baunack S, Diestel A, Holzapfel B, Schultz L and Fähler S 2010 Comparing properties of substrate-constrained and freestanding epitaxial Ni-Mn-Ga films *Acta Mater.* **58** 3415–21
[99] Ghahfarokhi M T, Casoli F, Minnert C, Bruns S, Bruder E, Cabassi R, Durst K, Gutfleisch O and Albertini F 2023 Effects of nanoindents on the martensitic transformation of Ni-Mn-Ga shape-memory Heusler films: a study by high-resolution imaging as a function of temperature *Acta Mater.* **245** 118603
[100] Zhang F, Taake C, Huang B, You X, Ojiyed H, Shen Q, Dugulan I, Caron L, van Dijk N and Brück E 2022 Magnetocaloric effect in the (Mn,Fe)$_2$(P,Si) system: from bulk to nano *Acta Mater.* **224** 117532
[101] Liu Y, Fu X, Yu Q, Zhang M and Liu J 2021 Significant reduction of phase-transition hysteresis for magnetocaloric

$(La_{1-x}Ce_x)_2Fe_{11}Si_2H$ alloys by microstructural manipulation *Acta Mater.* **207** 116687
[102] Andrade V M, Vivas R J C, Pedro S S, Tedesco J C G, Rossi A L, Coelho A A, Rocco D L and Reis M S 2016 Magnetic and magnetocaloric properties of $La_{0.6}Ca_{0.4}MnO_3$ tunable by particle size and dimensionality *Acta Mater.* **102** 49–55
[103] Trassinelli M *et al* 2014 Suppression of the thermal hysteresis in magnetocaloric MnAs thin film by highly charged ion bombardment *Appl. Phys. Lett.* **104** 081906
[104] Zhitomirsky M E 2003 Enhanced magnetocaloric effect in frustrated magnets *Phys. Rev.* B **67** 104421
[105] Koskelo E A C, Mukherjee P, Liu C, Hamilton A C S, Ong H S, Castelnovo C and Dutton S E 2023 Comparative study of magnetocaloric properties for Gd^{3+} compounds with different frustrated lattice geometries *PRX Energy* **2** 033005
[106] Zhang Y, Hao W, Lin J, Li H F and Li L 2024 Geometrically frustrated $Gd_2Ti_2O_7$ oxide: a comprehensive exploration of structural, magnetic, and magnetocaloric properties for cryogenic magnetic cooling applications *Acta Mater.* **272** 119946
[107] Das M, Roy S, Khan N and Mandal P 2018 Giant magnetocaloric effect in an exchange-frustrated $GdCrTiO_5$ antiferromagnet *Phys. Rev.* B **98** 104420
[108] Kumar J and Mukherjee K 2024 Enhanced cryogenic magnetocaloric performance and the existence of short-range magnetic correlations in frustrated diamond geometries *J. Appl. Phys.* **57** 295304
[109] Bramwell S T and Gingras M J P 2001 Spin ice state in frustrated magnetic pyrochlore materials *Science* **294** 1495–501
[110] Borzi R A, Gómez Albarracín F A, Rosales H D, Rossini G L, Steppke A, Prabhakaran D, Mackenzie A P, Cabra D C and Grigera S A 2016 Intermediate magnetization state and competing orders in $Dy_2Ti_2O_7$ and $Ho_2Ti_2O_7$ *Nat. Commun.* **7** 12592
[111] Sánchez-Alarcos V, Pérez-Landazábal J I, Recarte V, Lucia I, Vélez J and Rodríguez-Velamazán J A 2013 Effect of high-temperature quenching on the magnetostructural transformations and the long-range atomic order of Ni-Mn-Sn and Ni-Mn-Sb metamagnetic shape memory alloys *Acta Mater.* **61** 4676–82
[112] Unzueta I, López-García J, Sánchez-Alarcos V, Recarte V, Pérez-Landazábal J I, Rodríguez-Velamazán J A and Plazaola F 2017 ^{119}Sn Mössbauer spectroscopy for assessing the local stress and defect state towards the tuning of Ni-Mn-Sn alloys *Appl. Phys. Lett.* **110** 18
[113] Sánchez-Alarcos V, Recarte V, Pérez-Landazábal J I, Cesari E and Rodríguez-Velamazán J A 2014 Long -range atomic order and entropy change at the martensitic transformation in a Ni-Mn-In-Co metamagnetic shape memory alloy *Entropy* **16** 2756–67
[114] Sánchez-Alarcos V, Recarte V, Pérez-Landazábal J I, Gómez-Polo C and Rodríguez-Velamazán J A 2012 Role of magnetism on the martensitic transformation in Ni-Mn-based magnetic shape memory alloys *Acta Mater.* **60** 459–68
[115] Bruno N M, Yegin C, Karaman I, Chen J H, Ross J J H, Liu J and Li J 2014 The effect of heat treatments on $Ni_{43}Mn_{42}Co_4Sn_{11}$ meta-magnetic shape memory alloys for magnetic refrigeration *Acta Mater.* **74** 66–84
[116] Zhang M, Shao Y, Li C, Zhang Y, Sun W, Wei Z, Skokov K P, Liu J and Yan A 2023 High-performance $LaFe_{11.6}Si_{1.4}H$/Al composites for magnetic refrigeration: a good combination of magnetocaloric effect, mechanical properties, and thermal conductivity *J. Alloys Compd.* **962** 171123
[117] Cen D, Wang B, Chu R, Gong Y, Xu G, Chen F and Xu F 2020 Design of (Hf,Ta)Fe_2/Fe composite with zero thermal expansion covering room temperature *Scr. Mater.* **186** 331–5